High-order weighted essentially nonoscillatory finite-difference formulation of the lattice Boltzmann method in generalized curvilinear coordinates

Kazem Hejranfar,* Mohammad Hossein Saadat, and Sina Taheri
Aerospace Engineering Department, Sharif University of Technology, Iran
(Received 30 October 2015; revised manuscript received 14 December 2016; published 24 February 2017)

In this work, a high-order weighted essentially nonoscillatory (WENO) finite-difference lattice Boltzmann method (WENOLBM) is developed and assessed for an accurate simulation of incompressible flows. To handle curved geometries with nonuniform grids, the incompressible form of the discrete Boltzmann equation with the Bhatnagar-Gross-Krook (BGK) approximation is transformed into the generalized curvilinear coordinates and the spatial derivatives of the resulting lattice Boltzmann equation in the computational plane are solved using the fifth-order WENO scheme. The first-order implicit-explicit Runge-Kutta scheme and also the fourth-order Runge-Kutta explicit time integrating scheme are adopted for the discretization of the temporal term. To examine the accuracy and performance of the present solution procedure based on the WENOLBM developed, different benchmark test cases are simulated as follows: unsteady Taylor-Green vortex, unsteady doubly periodic shear layer flow, steady flow in a two-dimensional (2D) cavity, steady cylindrical Couette flow, steady flow over a 2D circular cylinder, and steady and unsteady flows over a NACA0012 hydrofoil at different flow conditions. Results of the present solution are compared with the existing numerical and experimental results which show good agreement. To show the efficiency and accuracy of the solution methodology, the results are also compared with the developed second-order central-difference finite-volume lattice Boltzmann method and the compact finite-difference lattice Boltzmann method. It is shown that the present numerical scheme is robust, efficient, and accurate for solving steady and unsteady incompressible flows even at high Reynolds number flows.

DOI: 10.1103/PhysRevE.95.023314

I. INTRODUCTION

In the last three decades, the lattice Boltzmann method (LBM) has become one a powerful technique to simulate fluid flow problems. In recent years, the LBM is used to simulate complex fluid flows such as incompressible flows, high-speed compressible flows, multiphase and multicomponent flows, magnetohydrodynamics, and so on, and it has been an attractive alternative computational technique to the traditional Navier-Stokes solvers. The simplicity of considering microscopic interactions for modeling of additional physical phenomena is the main advantage of the LBM. Specifically, because of its roots in statistical mechanics and kinetic theory, the LBM performs very well for flows where continuum assumptions break down. Historically the LBM evolved from the lattice gas automata (LGA) method, but later it was shown that it can be derived independently from the continuous Boltzmann equation by discretizing the velocity space [1].

In the lattice Boltzmann framework, macroscopic flow variables can be recovered from the dynamic evolution of particle distribution functions in the phase space. From a computational point of view, the solution of the LB equation seems to be easier than the Navier-Stokes equations for the fluid flow simulations. In fact, the LB equation is a simple linear hyperbolic equation which consists of only first-order derivatives and therefore it can be solved simply and efficiently by applying conventional numerical methods. Note that the Navier-Stokes equations contain both the first- and second-order derivatives and besides that, the convective terms in the Navier-Stokes equations are nonlinear, and nonlinearity is a source of numerical difficulty. Another advantage of the LBM over the Navier-Stokes equations is that the pressure in the incompressible Navier-Stokes solvers using the pressure-based methods should be obtained by solving a Poisson equation in an iterative manner that is very time consuming; however, the pressure in the LBM is calculated locally via an equation of state in an efficient manner. One can also solve the incompressible Navier-Stokes equations with the artificial compressibility method to obtain the pressure field. In [2], it has been shown that the simulated pressure fields from the LBM and the Navier-Stokes equations with the artificial compressibility method exhibit a significant difference and the LBM may be more accurate than the artificial compressibility method in capturing the pressure waves. Also, in [3] some features of the linkwise artificial compressibility method of Asinari *et al.* [4], in which the replacement of parts of the LBM algorithm by expressions deduced from finite-differencing the primitive variables is performed, are analyzed and discussed and alternative finite-difference expressions are proposed to improve the resulting simulations. So, in addition to the capability of the LBM to simulate complex physics, ease of programing and parallelization make this method very attractive in computational fluid dynamics.

In spite of the advantages of the LBM over Navier-Stokes flow solvers, it has some serious limitations too. In the standard LBM, which is based on the streaming and collision steps, the physical structure of the lattice is coupled to the velocity discretization of particle distribution functions; hence the method is restricted to uniform Cartesian grids with equal spacing. The use of a uniform mesh in the standard LBM greatly limits its applications to solve engineering practical problems with complex geometries. Another important limitation of the standard LBM is its inherent instability at high Reynolds number flows. To overcome the stability problem, some efforts have been made in the literature. One way is to

*khejran@sharif.edu

use the multi-relaxation-time method [5] or to implement the cascaded LBM [6] which improves the numerical stability of the LBM.

Another way to enhance the stability limits and accuracy of the LBM is to decouple the numerical mesh from the lattice structure and discretize space and time independently. He and Luo [1] have shown that the discretization of phase space and the physical space can be made independently. According to this idea, the other way to improve stability is to use the conventional ways to discretize the discrete Boltzmann equation (DBE) since the instability problem is closely related to strong coupling between time and space discretizations. In recent years, different traditional numerical methods such as finite-difference (FD) [7–16], finite-volume (FV) [17–21], finite-element (FE) [22–26], and spectral methods [27] have been used to improve the computational accuracy and efficiency of the LBM. These differential types of LB methods can overcome the difficulties encountered at high Reynolds number flows by using body-conforming, curvilinear meshes with clustering of grid points in critical zones.

For precisely predicting complex fluid flows, high-order accurate numerical methods have to be used; these methods reduce the number of grid points and the CPU time requirements compared to the other traditional low-order numerical methods. Achieving high-order accuracy in finite-difference methods is simple and straightforward compared to the other numerical methods. Since the LB equation has a simpler formulation than the Navier-Stokes equations, the implementation of high-order accurate finite-difference methods to solve the LB equation seems to be easier and high-order accurate FDLBM can be considered as an alternative to the high-order accurate FD Navier-Stokes solvers.

Most of the previous FDLBM developed in the literature are based on usual finite-difference schemes with second-order accuracy. In FDLBM, one can apply high-order accurate numerical methods for improving the accuracy and performance of the solution. Recently, the high-order compact finite-difference method has been applied to the LBM (CFDLBM) and it has been shown that it improves the capability of the LBM in modeling different fluid flow problems [15,16]. Although the CFDLBM has shown an improvement in the LBM, because there is no built-in upwinding, a filtering procedure has to be applied to stabilize the numerical solution. Thus, it is desirable to apply an accurate and practical numerical method based on the finite-difference LBM that does not contain this deficiency.

Although the FDLBM has better stability than the standard LBM, it still suffers from numerical instability, especially when the relaxation time is small (i.e., Reynolds number is high). From a numerical point of view, at small relaxation time, the LB equation with the Bhatnagar-Gross-Krook (BGK) approximation becomes stiff, which means that it requires a very small time step $\Delta t \approx O(\tau)$ to maintain the numerical stability. The requirement of small Δt is particularly restrictive in the case of flows with high Reynolds numbers where τ is very small [28]. One of the simple and effective ways to treat the stiff equations is to use the implicit-explicit (IMEX) Runge-Kutta scheme for the time discretization. In this method, the collision term which is the source of instability and stiffness is treated implicitly and the convective terms are treated explicitly. With the IMEX time discretization, the restriction of $\Delta t \approx O(\tau)$ due to the explicit approximation of the collision term can be relaxed; however, the explicit discretization of the convective terms imposes a stability criterion on Δt through the Courant-Friedrichs-Lewy (CFL) condition, i.e., $\mathrm{CFL} = \Delta t / \min(\Delta x, \Delta y) < 1$.

The main objective of this paper is to implement the high-order WENO finite-difference scheme with the incompressible LBM in the generalized curvilinear coordinates with nonuniform grids. The WENO scheme has already been applied to the compressible LB equation to simulate compressible flows [29,30] and this scheme has not been applied and assessed to the incompressible LB equation in the literature yet. The upwind nature of the WENO scheme guarantees that the scheme can readily be used in applications involving high Reynolds number flows or flows with strong shear. To handle curved geometries with nonuniform grids the incompressible LB equation is transformed into the generalized curvilinear coordinates. Herein the spatial derivatives in the incompressible form of the LB equation in the computational plane are discretized by using the fifth-order WENO finite-difference scheme. The temporal term is solved based on the first-order IMEX scheme and also the fourth-order explicit Runge-Kutta scheme. The accuracy and efficiency of the WENOLBM are examined by solving different benchmark incompressible flow problems at different conditions. Results obtained by applying the WENOLBM are compared with those of the developed second-order finite-volume lattice Boltzmann method (FVLBM) and also the fourth-order compact finite-difference lattice Boltzmann method (CFDLBM).

The paper is organized as follows: In Sec. II, the LB equation for the two-dimensional (2D) incompressible flows based on the pressure distribution function is presented and it is transformed into the generalized curvilinear coordinates in Sec. III. In Sec. IV, the spatial and time discretization schemes are given. The implementation of boundary conditions is presented in Sec. V. Section VI is devoted to presenting the results obtained by applying the WENOLBM and FVLBM for different 2D test cases. Finally, some conclusions are given in Sec. VII.

II. GOVERNING EQUATIONS

The governing equation in the lattice Boltzmann method is the continuous Boltzmann equation

$$\frac{\partial f}{\partial t} + \boldsymbol{e} \cdot \nabla f = \Omega, \tag{1}$$

in which f is the particle distribution function, e is the particle velocity, and Ω is the collision term between particles. According to the Bhatnagar-Gross-Krook (BGK) approximation, the collision between particles drives the particle distribution function toward an equilibrium distribution f^{eq} with a single relaxation time τ [31],

$$\Omega = \frac{-1}{\tau}(f - f^{\mathrm{eq}}). \tag{2}$$

A two-dimensional square lattice model with nine velocity directions (D2Q9) is employed to discretize Eq. (1) in the lattice configuration. Therefore, the lattice Boltzmann (LB) equation for the particle distribution function f_α in the

direction of microscopic velocity $\boldsymbol{e}_\alpha$ may be written as

$$\frac{\partial f_\alpha}{\partial t} + \boldsymbol{e}_\alpha \cdot \nabla f_\alpha = -\frac{1}{\tau}\left(f_\alpha - f_\alpha^{\mathrm{eq}}\right),\ \alpha = 0,1,\ldots,8, \quad (3)$$

where the subscript α denotes the direction of the particle speed. In the D2Q9 discrete Boltzmann model, the microscopic velocities are given as

$$\boldsymbol{e}_\alpha = (e_{\alpha x}, e_{\alpha y}) = \begin{cases} (0,0) & \alpha = 0 \\ \left[\cos\left(\frac{\alpha-1}{2}\pi\right),\ \sin\left(\frac{\alpha-1}{2}\pi\right)\right] & \alpha = 1,2,3,4 \\ \left[\cos\left(\frac{\alpha-5}{2}\pi + \frac{1}{4}\pi\right),\ \sin\left(\frac{\alpha-5}{2}\pi + \frac{1}{4}\pi\right)\right]\sqrt{2} & \alpha = 5,6,7,8 \end{cases}. \quad (4)$$

The equilibrium distribution function f^{eq} must be chosen such that the mass and momentum remain conserved and the incompressible Navier-Stokes equations are satisfied through the Chapman-Enskog expansion. The incompressible form of the LB equation used herein is based on the model given by He and Luo [32]. They introduced a local pressure distribution function, redefining the density distribution in the LB equation by the fact that the error terms in the order of $O(M^2)$ [where $M = u_{\mathrm{ref}}/c_s$ is the Mach number in which u_{ref} is the reference (characteristic) macroscopic velocity and c_s is the speed of sound] are explicitly removed from the equilibrium distribution function. In this formulation, the fluid density is not calculated in the simulations and the incompressible form of the LB equation solves the pressure in the computational domain as the independent variable. The resulting equation of the equilibrium distribution function f_α^{eq} is defined as

$$f_\alpha^{\mathrm{eq}} = w_\alpha\left\{p + p_0\left[3\frac{\boldsymbol{e}_\alpha \cdot \boldsymbol{u}}{c^2} + \frac{9}{2}\frac{(\boldsymbol{e}_\alpha \cdot \boldsymbol{u})^2}{c^4} - \frac{3}{2}\frac{|\boldsymbol{u}|^2}{c^2}\right]\right\}, \quad (5)$$

where $\boldsymbol{u} = (u,v)$ is the macroscopic velocity vector in Cartesian coordinates and the weight coefficient w_α for the D2Q9 model is given by

$$\begin{aligned} w_0 &= 4/9, \\ w_1 &= \cdots = w_4 = 1/9, \\ w_5 &= \cdots = w_8 = 1/36. \end{aligned} \quad (6)$$

The macroscopic fluid pressure p and the macroscopic velocity vector $\boldsymbol{u}$ are obtained from the following relations:

$$p = \sum_\alpha f_\alpha, \quad p_0\boldsymbol{u} = \sum_\alpha \boldsymbol{e}_\alpha f_\alpha, \quad (7)$$

where $p_0 = c_s^2\rho_0$ and $c_s = 1/\sqrt{3}$ [33] in the LBM, and ρ_0 is the constant density of the fluid.

By applying the Chapman-Enskog expansion to the DBE, the incompressible Navier-Stokes equations can be derived from the incompressible LB model,

$$\frac{1}{c_s^2}\frac{\partial p}{\partial t} + \nabla \cdot \boldsymbol{u} = 0, \quad (8)$$

$$\frac{\partial \boldsymbol{u}}{\partial t} + \boldsymbol{u} \cdot \nabla \boldsymbol{u} = -\nabla p + \nu\nabla^2\boldsymbol{u}, \quad (9)$$

where ν is the kinematic viscosity of the fluid and the relation for the relaxation time τ in the finite-difference LB model is given by [10]

$$\tau = \frac{\nu}{c_s^2}. \quad (10)$$

III. TRANSFORMATION TO GENERALIZED CURVILINEAR COORDINATES

In the generalized curvilinear coordinates, the physical and computational domains are denoted by (x,y) and (ξ,η), respectively:

$$\xi = \xi(x,y), \quad \eta = \eta(x,y). \quad (11)$$

The relationship between the physical and computational domains satisfies the following condition:

$$\begin{bmatrix} \xi_x & \xi_y \\ \eta_x & \eta_y \end{bmatrix} = \frac{1}{J}\begin{bmatrix} y_\eta & -x_\eta \\ -y_\xi & x_\xi \end{bmatrix}, \quad (12)$$

where J is the Jacobian of the transformation given by

$$J = x_\xi y_\eta - x_\eta y_\xi. \quad (13)$$

Using the chain rule, the convection term in Eq. (3) can be rewritten as

$$\begin{aligned} \boldsymbol{e}_\alpha \cdot \nabla f &= e_{\alpha x}\frac{\partial f_\alpha}{\partial x} + e_{\alpha y}\frac{\partial f_\alpha}{\partial y} \\ &= e_{\alpha x}\left(\frac{\partial f_\alpha}{\partial \xi}\xi_x + \frac{\partial f_\alpha}{\partial \eta}\eta_x\right) + e_{\alpha y}\left(\frac{\partial f_\alpha}{\partial \xi}\xi_y + \frac{\partial f_\alpha}{\partial \eta}\eta_y\right) \\ &= (e_{\alpha x}\xi_x + e_{\alpha y}\xi_y)\frac{\partial f_\alpha}{\partial \xi} + (e_{\alpha x}\eta_x + e_{\alpha y}\eta_y)\frac{\partial f_\alpha}{\partial \eta} \\ &= \tilde{e}_{\alpha\xi}\frac{\partial f_\alpha}{\partial \xi} + \tilde{e}_{\alpha\eta}\frac{\partial f_\alpha}{\partial \eta}, \end{aligned} \quad (14)$$

where $\tilde{\boldsymbol{e}}_\alpha = (\tilde{e}_{\alpha\xi}, \tilde{e}_{\alpha\eta}) = (e_{\alpha x}\xi_x + e_{\alpha y}\xi_y, e_{\alpha x}\eta_x + e_{\alpha y}\eta_y)$ is the microscopic contravariant velocity vectors in the computational plane. Then, in the generalized coordinates, Eq. (3) can be written as

$$\frac{\partial f_\alpha}{\partial t} = -\left(\tilde{e}_{\alpha\xi}\frac{\partial f_\alpha}{\partial \xi} + \tilde{e}_{\alpha\eta}\frac{\partial f_\alpha}{\partial \eta}\right) - \frac{1}{\tau}\left(f_\alpha - f_\alpha^{\mathrm{eq}}\right), \quad \alpha = 0,1,\ldots,8. \quad (15)$$

IV. DISCRETIZATION PROCEDURE

In the present study, we apply the fifth-order finite-difference weighted essentially nonoscillatory (WENO) scheme to the spatial derivatives in the LB equation in the computational domain and the first-order implicit-explicit Runge-Kutta scheme and the fourth-order explicit Runge-Kutta scheme are applied for the temporal discretization to achieve an accurate and efficient incompressible flow solver. A second-order finite-volume LB solver is also developed for the assessment of the WENO solver.

A. Spatial discretization

1. Fifth-order WENO scheme

The natural implementation of upwinding in the WENO scheme is to use the signs of microscopic contravariant velocity in front of the spatial derivatives in Eq. (15). The semidiscretized form of Eq. (15) is

$$\frac{\partial f_\alpha}{\partial t}+\frac{\tilde{e}_{\alpha\xi}}{\Delta\xi}(f_{\alpha,i+1/2,j}-f_{\alpha,i-1/2,j})+\frac{\tilde{e}_{\alpha\eta}}{\Delta\eta}(f_{\alpha,i,j+1/2}-f_{\alpha,i,j-1/2})=-\frac{1}{\tau}\left(f_\alpha-f_\alpha^{\mathrm{eq}}\right), \quad (16)$$

where i and j are indices of each cell and $f_{\alpha,i\pm1/2,j}$, $f_{\alpha,i,j\pm1/2}$ are computed based on the fifth-order WENO scheme as follows [29,34]:

$$f_{\alpha,i+1/2}=\sum_{k=1}^{3}\omega_k f_{\alpha,i+1/2}^{(k)}, \quad (17)$$

where $f_{\alpha,i+1/2}^{(k)}$ is a third-order approximation of f (and if $\tilde{e}_{\alpha\xi}>0$); we have

$$\begin{aligned} f_{\alpha,i+1/2}^{(1)}&=\tfrac{1}{3}f_{\alpha,i-2}-\tfrac{7}{6}f_{\alpha,i-1}+\tfrac{11}{6}f_{\alpha,i},\\ f_{\alpha,i+1/2}^{(2)}&=-\tfrac{1}{6}f_{\alpha,i-1}+\tfrac{5}{6}f_{\alpha,i}+\tfrac{1}{3}f_{\alpha,i+1},\\ f_{\alpha,i+1/2}^{(3)}&=\tfrac{1}{3}f_{\alpha,i}+\tfrac{5}{6}f_{\alpha,i+1}-\tfrac{1}{6}f_{\alpha,i+2}. \end{aligned} \quad (18)$$

The nonlinear weights ω_k in Eq. (17) are

$$\omega_l=\widetilde{\omega}_l\Big/\sum_{l=1}^{3}\widetilde{\omega}_l,\quad \widetilde{\omega}_l=\frac{\gamma_l}{(\varepsilon+\beta_l)^2}, \quad (19)$$

where the smoothness indicators $\beta_l (l=1,2,3)$ are given by

$$\begin{aligned} \beta_1&=\tfrac{13}{12}(f_{\alpha,i-2}-2f_{\alpha,i-1}+f_{\alpha,i})^2+\tfrac{1}{4}(f_{\alpha,i-2}-4f_{\alpha,i-1}+f_{\alpha,i})^2,\\ \beta_2&=\tfrac{13}{12}(f_{\alpha,i-1}-2f_{\alpha,i}+f_{\alpha,i+1})^2+\tfrac{1}{4}(f_{\alpha,i-1}-f_{\alpha,i+1})^2,\\ \beta_3&=\tfrac{13}{12}(f_{\alpha,i}-2f_{\alpha,i+1}+f_{\alpha,i+2})^2+\tfrac{1}{4}(3f_{\alpha,i}-4f_{\alpha,i+1}+f_{\alpha,i+2})^2, \end{aligned} \quad (20)$$

and the linear weights γ_l are $\gamma_1=0.1$, $\gamma_2=0.6$, and $\gamma_3=0.3$. Finally, ε is a small positive number used to avoid the denominator becoming zero and is typically chosen to be $\varepsilon=10^{-6}$.

Equation (17) is applied in the computational domain for the grid points $i=3,\ldots,I_{\max}-2$ for each j. At the near boundary points, the third-order reconstructions for $f_{\alpha,i+1/2}$ are used as follows:

$$\begin{aligned} &\text{for } i=2: f_{\alpha,i+1/2}=-\tfrac{1}{6}f_{\alpha,i-1}+\tfrac{5}{6}f_{\alpha,i}+\tfrac{1}{3}f_{\alpha,i+1},\\ &\text{for } i=I_{\max}-1: f_{\alpha,i+1/2}=\tfrac{1}{3}f_{\alpha,i-2}-\tfrac{7}{6}f_{\alpha,i-1}+\tfrac{11}{6}f_{\alpha,i}, \end{aligned} \quad (21)$$

and if $\tilde{e}_{\alpha\xi}<0$, $f_{\alpha,i+1/2}$ is constructed symmetrically as above about $i+\frac{1}{2}$. The calculation of $f_{\alpha,i,j\pm1/2}$ is performed in the same manner. It should be noted that the metrics $(x_\xi, y_\xi, \ldots)$ appearing in Eq. (15) are also calculated by using the fourth-order central finite-difference formula.

2. Second-order finite-volume scheme

In order to assess the accuracy and performance of the WENOLBM, we have also developed a second-order finite-volume lattice Boltzmann method (FVLBM). The selected approach is a flux averaging cell-centered finite-volume scheme based on the quadrilateral elements. By integrating Eq. (3) over each element, the governing equation is described as

$$\int_s\left[\frac{\partial f_\alpha}{\partial t}+\mathbf{e}_\alpha\cdot\nabla f_\alpha+\frac{1}{\tau}\left(f_\alpha-f_\alpha^{\mathrm{eq}}\right)\right]ds=0,\quad \alpha=0,1,\ldots,8. \quad (22)$$

The integration for the convective term is performed by applying Green's theorem and using the flux averaging on the faces as follows:

$$\begin{aligned} \int_s(\mathbf{e}_\alpha\cdot\nabla f_\alpha)ds&=\int_s\left(e_{\alpha x}\frac{\partial f_\alpha}{\partial x}+e_{\alpha y}\frac{\partial f_\alpha}{\partial y}\right)ds\\ &=\oint_{\text{around cell}}(e_{\alpha x}f_\alpha dy-e_{\alpha y}f_\alpha dx)\\ &\approx\sum_{\text{all faces}}\frac{[f_\alpha]_{\text{cell}}+[f_\alpha]_{\text{neighbor}}}{2}\\ &\quad\times(e_{\alpha x}dy-e_{\alpha y}dx), \end{aligned} \quad (23)$$

where $e_{\alpha x}$ and e_{ay} are constant. With the assumption of f_α and f_α^{eq} to be constant over each cell, the discretized form of Eq. (22) is given by

$$\left[\frac{\partial f_\alpha}{\partial t}\right]A=-\sum_{\text{all faces}}\frac{[f_\alpha]_{\text{cell}}+[f_\alpha]_{\text{neighbor}}}{2}\times(e_{\alpha x}dy-e_{\alpha y}dx)-\frac{A}{\tau}\left(f_\alpha-f_\alpha^{\mathrm{eq}}\right), \quad (24)$$

where A is the area of the element. In flux averaging schemes, spurious oscillations are inherited in the numerical solution; then the artificial dissipation terms should be added to the formulation to stabilize the numerical simulation. The fourth-order artificial dissipation as

$$D^{(4)}f_\alpha=\varepsilon_d\left[(\nabla\Delta)_x^2+(\nabla\Delta)_y^2\right]f_\alpha \quad (25)$$

is added to Eq. (24), where ε_d is the damping factor. In Eq. (25) the gradient operator is discretized in the x and y directions as follows:

$$\begin{aligned} (\nabla\Delta)_x^2 f_{\alpha,i,j}&=f_{\alpha,i+2,j}-4f_{\alpha,i+1,j}+6f_{\alpha,i,j}-4f_{\alpha,i-1,j}+f_{\alpha,i-2,j},\\ (\nabla\Delta)_y^2 f_{\alpha,i,j}&=f_{\alpha,i,j+2}-4f_{\alpha,i,j+1}+6f_{\alpha,i,j}-4f_{\alpha,i,j-1}+f_{\alpha,i,j-2}. \end{aligned} \quad (26)$$

B. Temporal discretization

1. Fourth-order explicit Runge-Kutta (RK4) scheme

For stiff equations, all the explicit methods have stability restriction and the computations tend to become very inefficient because the time step size dictated by the stability requirements

is very small. Among the explicit methods, the fourth-order Runge-Kutta methods have good stability and are suitable for the accurate calculation of unsteady flows. The semidiscretized form of Eqs. (15) or (24) can be written as follows:

$$\frac{df_\alpha}{dt} = R(f_\alpha), \tag{27}$$

where $R(f_\alpha)$ is the operator defined by the right-hand side of Eqs. (15) or (24). The explicit fourth-order Runge-Kutta scheme is expressed as

$$\begin{aligned} f_\alpha^0 &= f_\alpha^t, \\ f_\alpha^k &= f_\alpha^0 + \lambda_k \Delta t R^{k-1}(f_\alpha), \quad k=1,2,3,4 \quad \lambda_k = \tfrac{1}{4}, \tfrac{1}{3}, \tfrac{1}{2}, 1, \\ f_\alpha^{t+\Delta t} &= f_\alpha^4. \end{aligned} \tag{28}$$

2. *Implicit-explicit (IMEX) Runge-Kutta scheme*

The IMEX Runge-Kutta scheme consists of the implicit time discretization of the collision term and the explicit one for the convective terms and in this scheme the restriction of $\Delta t \leqslant 2\tau$ can be relaxed and the only restriction on Δt is due to the explicit discretization of the convective terms. The scheme is expressed as [29]

$$\begin{aligned} f_\alpha^{(j)} = f_\alpha^n &- \Delta t \sum_{k=1}^{j-1} \tilde{m}_{jk} \left(e_\alpha \cdot \nabla f_\alpha^{(k)}\right) \\ &- \Delta t \sum_{k=1}^{j} m_{jk} \frac{f_\alpha^{(k)} - f_\alpha^{\mathrm{eq}(k)}}{\tau}, \end{aligned} \tag{29}$$

$$\begin{aligned} f_\alpha^{n+1} = f_\alpha^n &- \Delta t \sum_{j=1}^{r} \tilde{n}_j \left(e_\alpha \cdot \nabla f_\alpha^{(k)}\right) \\ &- \Delta t \sum_{j=1}^{r} n_j \frac{f_\alpha^{(k)} - f_\alpha^{\mathrm{eq}(k)}}{\tau}, \end{aligned} \tag{30}$$

where $f_\alpha^{(j)}$ and $f_\alpha^{\mathrm{eq}(j)}$ are the jth stage of the particle distribution function and the equilibrium particle distribution function, respectively. Here, r is the stage number and two $r \times r$ matrices $\tilde{M} = \tilde{m}_{jk}$ and $M = m_{jk}$, and the two vectors $\tilde{n}_j$ and n_j characterize the IMEX Runge-Kutta scheme. The characteristic of the collision invariants ϕ of the LBM provides us with a simple trick to update $f_\alpha^{(j)}$. One can rewrite Eq. (29) as [29]

$$\begin{aligned} \sum_{\alpha=0}^{8} f_\alpha^{(j)} \phi = \sum_{\alpha=0}^{8} f_\alpha^n \phi &- \Delta t \sum_{k=1}^{j-1} \tilde{m}_{jk} \left[\sum_{\alpha=0}^{8} \left(e_\alpha \cdot \nabla f_\alpha^{(k)}\right) \phi \right] \\ &- \Delta t \sum_{k=1}^{j} \frac{m_{jk}}{\tau} \left[\sum_{\alpha=0}^{8} \left(f_\alpha^{(k)} - f_\alpha^{\mathrm{eq}(k)}\right) \phi \right], \end{aligned} \tag{31}$$

and from

$$\sum_{\alpha=0}^{8} \left(f_\alpha^{(k)} - f_\alpha^{\mathrm{eq}(k)}\right) \phi = 0 \tag{32}$$

we can further obtain

$$\sum_{\alpha=0}^{8} f_\alpha^{(j)} \phi = \sum_{\alpha=0}^{8} f_\alpha^n \phi - \Delta t \sum_{k=1}^{j-1} \tilde{m}_{jk} \left[\sum_{\alpha=0}^{8} \left(e_\alpha \cdot \nabla f_\alpha^{(k)}\right) \phi \right], \tag{33}$$

where ϕ can be $1, e_{\alpha x}$ and $e_{\alpha y}$. With this equation, the jth stage macroscopic variables $(u^{(j)}, v^{(j)}, p^{(j)})$ can be calculated, so one can update corresponding $f_\alpha^{\mathrm{eq}(j)}$. Therefore, $f_\alpha^{(j)}$ can be given explicitly as

$$f_\alpha^{(j)} = \frac{f_\alpha^n - \Delta t \sum_{k=1}^{j-1} \tilde{m}_{jk} \left(e_\alpha \cdot \nabla f_\alpha^{(k)}\right) - \Delta t \sum_{k=1}^{j-1} m_{jk} \frac{f_\alpha^{(k)} - f_\alpha^{\mathrm{eq}(k)}}{\tau} + \Delta t m_{jj} f_\alpha^{\mathrm{eq}(j)}/\tau}{1 + \frac{\Delta t}{\tau} m_{jj}}. \tag{34}$$

Thus, owing to the characteristic of the collision invariants in the LBM, no iteration is needed in practice.

The IMEX schemes are usually represented by a double Butcher's tableau as follows:

$$\begin{array}{c|c} \tilde{M} \\ \hline \tilde{n} \end{array} \qquad \begin{array}{c|c} M \\ \hline n \end{array}$$

In this study, we use a simple two-stage first-order IMEX Runge-Kutta scheme as follows:

$$\begin{array}{c|cc} 0 & 0 & 0 \\ 1 & 0 & 0 \\ \hline & 1 & 0 \end{array} \qquad \begin{array}{c|cc} 0 & 0 & 0 \\ 0 & 1 & \\ \hline & 0 & 1 \end{array}$$

V. BOUNDARY CONDITIONS IMPLEMENTATION

In the LB equation, the boundary conditions must be specified in terms of the distribution function f_α; however, f_α is not given at the boundaries; therefore a special treatment should be utilized for calculating its value based on the macroscopic variables at each boundary. Here, the distribution function at each boundary is written as follows:

$$f_\alpha = f_\alpha^{\mathrm{eq}} + f_\alpha^{\text{non-eq}}, \tag{35}$$

where f_α^{eq} is calculated by Eq. (5) with the use of the specified or extrapolated macroscopic variables at the desired boundary. At the inlet and on the wall boundary with no slip condition, the velocity components are known and to calculate the pressure at the boundary, the one-sided finite-difference extrapolation is used to discretize $\frac{\partial p}{\partial \eta} = 0$:

$$p_1 = \tfrac{1}{125}(240p_2 - 180p_3 + 80p_4 - 15p_5). \tag{36}$$

At the outlet, the pressure is set to a fixed value and the same extrapolation is used for the velocity components.

The nonequilibrium part of distribution function $f_\alpha^{\text{non-eq}}$ at the boundaries can be computed using the one-sided fourth-order finite-difference approximation of the formula

$\frac{\partial^2 f_\alpha^{\text{non-eq}}}{\partial \xi^2} = 0$ as follows:

$$f_{\alpha,1}^{\text{non-eq}} = \tfrac{1}{180}\left(616 f_{\alpha,2}^{\text{non-eq}} - 856 f_{\alpha,3}^{\text{non-eq}} + 624 f_{\alpha,4}^{\text{non-eq}} - 244 f_{\alpha,5}^{\text{non-eq}} + 40 f_{\alpha,6}^{\text{non-eq}}\right), \quad (37)$$

where the nonequilibrium distribution function is defined as $f_\alpha^{\text{non-eq}} = f_\alpha - f_\alpha^{\text{eq}}$.

VI. NUMERICAL RESULTS

To investigate the accuracy and robustness of the high-order numerical scheme (WENOLBM) applied, the solution algorithm is used to simulate different steady and unsteady flow problems. Different benchmark problems are considered for verifying the present computations and demonstrating the stability, accuracy, and efficiency of the solution algorithm: unsteady Taylor-Green vortex, unsteady doubly periodic shear layer flow, steady flow in a 2D cavity, steady cylindrical Couette flow, steady flow over a 2D circular cylinder, and steady and unsteady flows over a NACA0012 hydrofoil at different flow conditions. Results obtained for these test cases are compared with those of the developed second-order finite-volume lattice Boltzmann method (FVLBM) and also the available numerical and experimental results. All the present computations are performed on a computer with an Intel core i7-740QM processor, 1.73 GHz, with a 64-bit operating system.

A. Taylor-Green vortex problem

The Taylor-Green vortex decay problem has been widely used for the verification of incompressible flow solvers. This problem is solved here to demonstrate the accuracy and efficiency of the WENO finite-difference lattice Boltzmann method applied. The two-dimensional problem is introduced by Taylor [35] based on the incompressible Navier-Stokes equations in terms of the stream function and the vorticity variable. The exact solution of this unsteady problem is known as

$$u(x,y,t) = -u_{\text{ref}} \cos(N_1 x)\sin(N_2 y) e^{-\nu t (N_1^2+N_2^2)},$$
$$v(x,y,t) = \frac{N_1}{N_2} u_{\text{ref}} \sin(N_1 x)\cos(N_2 y) e^{-\nu t (N_1^2+N_2^2)},$$
$$p(x,y,t) = p_0 - \frac{1}{4}\rho_0 u_{\text{ref}}^2 \left[\cos(2N_1 x) + \left(\frac{N_1}{N_2}\right)^2 \cos(2N_2 y)\right] \times e^{-2\nu t (N_1^2+N_2^2)} \quad (38)$$

where u_{ref} is the initial velocity magnitude, ν is the kinematic viscosity, and $N_1 = 2$ and $N_2 = 2$ are the wave numbers in the x and y directions. Periodic boundary conditions are applied to all boundaries at the four sides of the domain ($0 \leqslant x \leqslant L$, $0 \leqslant y \leqslant L$, $L = 2\pi$). The analytical initial conditions for the velocity and pressure fields are obtained by setting $t = 0$ in Eq. (38).

Figure 1 indicates the computed Taylor's array of vortices with $\text{Re} = u_{\text{ref}} L/\upsilon = 10\pi$ at the dimensional time $t = 10$. As shown in this figure, the number of vortices is defined by $2 \times N_i$ in each direction. The present computations using the high-order WENO finite-difference LBM (WENOLBM) for the normalized velocity components $(u/u_{\text{ref}}, v/u_{\text{ref}})$ at the midlines $y = \pi$ and $x = \pi$, respectively, are compared with the analytical solution and the second-order finite-volume LBM (FVLBM) at $t = 10$. It is observed that the WENOLBM solver gives more accurate results than the FVLBM solver for the same number of grid points.

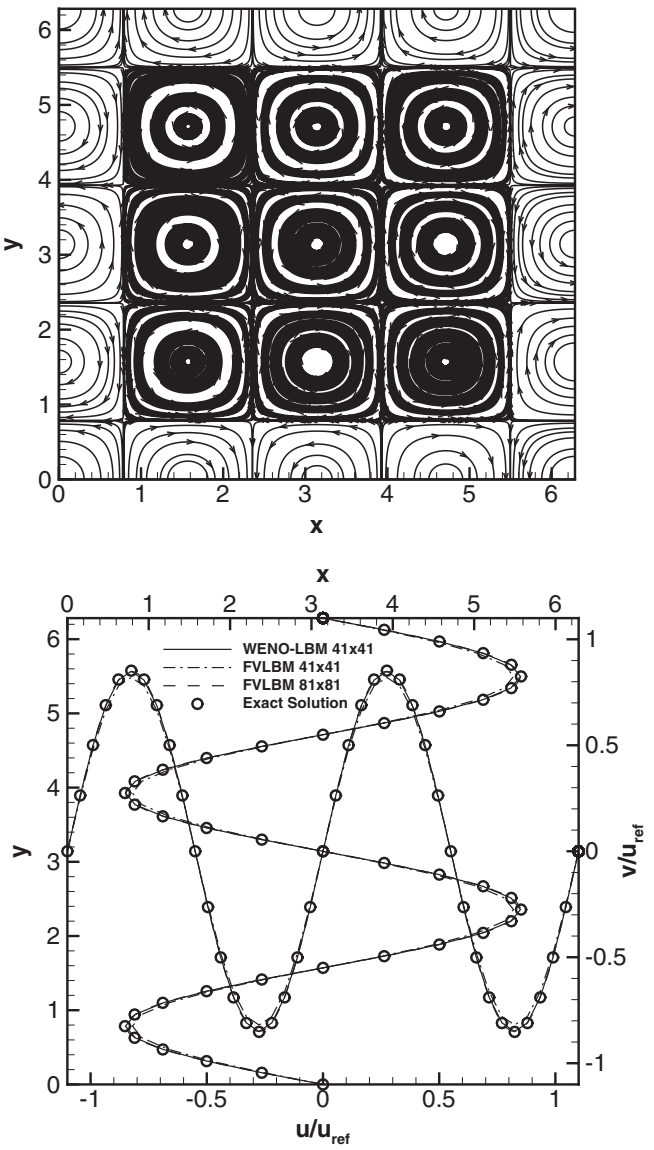

FIG. 1. Computed flow field shown by streamlines (top) and comparison of velocity profiles (bottom) for Taylor-Green vortex problem with $\text{Re} = 10\pi$ and $t = 10$.

The order of accuracy of the present numerical scheme is calculated for this problem for three reference velocity values, $u_{\text{ref}} = 0.1$, 0.01, and $u_{\text{ref}} = 0.001$ and the calculations are performed for the five computational grids, namely, (11×11), (21×21),(41×41), (81×81), and (161×161) at the Reynolds number $\text{Re} = 10\pi$ and $t = 10$. The error is calculated based on the L_2 norm of the u-velocity profile compared with the analytical solution and also that of the most refined grid. The results in Table I show that a small value of reference velocity leads to a more accurate solution due to decreasing the compressibility effects. The order of accuracy of the solution obtained is 3.48, 4.3, and 5.03

TABLE I. Order of accuracy of the solution based on the L_2 norm of u-velocity profile for Taylor-Green vortex problem with Re $= 10\pi$ at $t = 10$.

		Grid	Δy	$\log_{10}(\Delta y)$	$\log_{10}(L_2$ norm[Error])
$u_{\text{ref}} = 0.1$	Compared with the most refined grid (161×161)	(11×11)	$2\pi/10$	**–0.2018**	**–0.9286**
		(21×21)	$2\pi/20$	**–0.5028**	**–1.6745**
		(41×41)	$2\pi/40$	**–0.8038**	**–3.0542**
		(81×81)	$2\pi/80$	**–1.1049**	**–4.6529**
		Order of accuracy			**∼4.81**
	Compared with the analytical solution	(11×11)	$2\pi/10$	**–0.2018**	**–0.9285**
		(21×21)	$2\pi/20$	**–0.5028**	**–1.6742**
		(41×41)	$2\pi/40$	**–0.8038**	**–3.0077**
		(81×81)	$2\pi/80$	**–1.1049**	**–3.9725**
		Order of accuracy			**∼3.48**
$u_{\text{ref}} = 0.01$	Compared with the most refined grid (161×161)	(11×11)	$2\pi/10$	**–0.2018**	**–0.3243**
		(21×21)	$2\pi/20$	**–0.5028**	**–1.2294**
		(41×41)	$2\pi/40$	**–0.8038**	**–2.7593**
		(81×81)	$2\pi/80$	**–1.1049**	**–4.2331**
		Order of accuracy			**∼4.85**
	Compared with the analytical solution	(11×11)	$2\pi/10$	**–0.2018**	**–0.3243**
		(21×21)	$2\pi/20$	**–0.5028**	**–1.2300**
		(41×41)	$2\pi/40$	**–0.8038**	**–2.8394**
		(81×81)	$2\pi/80$	**–1.1049**	**–4.0552**
		Order of accuracy			**∼4.3**
$u_{\text{ref}} = 0.001$	Compared with the most refined grid (161×161)	(11×11)	$2\pi/10$	**–0.2018**	**–0.3696**
		(21×21)	$2\pi/20$	**–0.5028**	**–1.5526**
		(41×41)	$2\pi/40$	**–0.8038**	**–3.0343**
		(81×81)	$2\pi/80$	**–1.1049**	**–4.5463**
		Order of accuracy			**∼4.9**
	Compared with the analytical solution	(11×11)	$2\pi/10$	**–0.2018**	**–0.3695**
		(21×21)	$2\pi/20$	**–0.5028**	**–1.5528**
		(41×41)	$2\pi/40$	**–0.8038**	**–3.0405**
		(81×81)	$2\pi/80$	**–1.1049**	**–4.5737**
		Order of accuracy			**∼5.03**

by calculating the error based on the L_2 norm of the u-velocity profile compared with the analytical solution for the reference velocities $u_{\text{ref}} = 0.1$, 0.01, and 0.001, respectively. The present study shows that the fifth-order accuracy of the numerical method implemented is verified by considering a small value of the reference velocity for both ways of calculating the solution error. Note that the fifth-order accuracy of the numerical method applied is achieved independently of the value of the reference velocity when the error is calculated based on the solution of the most refined grid. Figure 2 shows the L_2-norm error of the solution obtained by the WENOLBM compared with the FVLBM for the Taylor vortex problem with $u_{\text{ref}} = 0.001$. It is observed that the WENOLBM is more accurate than the FVLBM by considering the same number of grid points and the FVLBM requires a higher number of grid points to provide the same accuracy achieved by applying the WENOLBM. To further assess the accuracy of the solution method applied, the Taylor vortex problem is also simulated on the nonunity aspect ratio grids for different grid sizes at Re $= 10\pi$ and $t = 10$. The corresponding errors based on the L_2 norm of the μ-velocity profile compared with the analytical solution are given in Table II which verifies that by decreasing the reference velocity, the desired order of the accuracy can be achieved even for the nonunity aspect ratio grids.

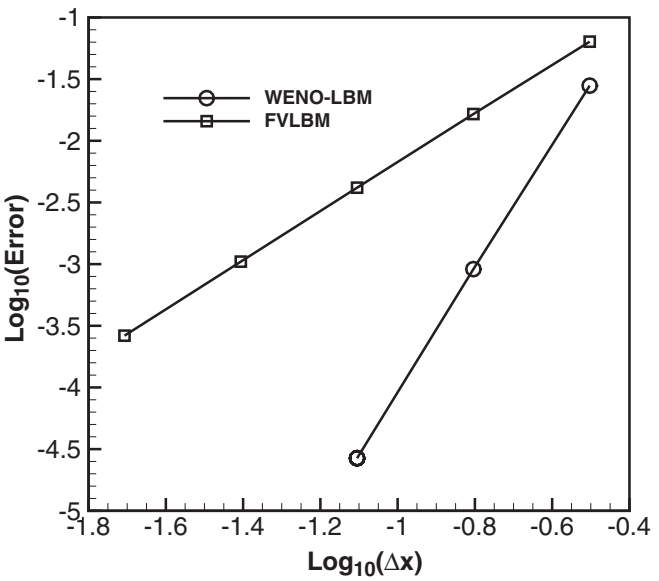

FIG. 2. Comparison of L_2-norm error of the solution for Taylor-Green vortex problem at Re $= 10\pi$ and $t = 10$ with $u_{\text{ref}} = 0.001$.

TABLE II. Order of accuracy of the solution based on the L_2 norm of the u-velocity profile for the Taylor-Green vortex problem with $\mathrm{Re} = 10\pi$ at $t = 10$ on nonuniform grids.

	Grid	Δy	$\log_{10}(\Delta y)$	$\log_{10}(L_2\,\mathrm{norm})$
$u_{\mathrm{ref}} = 0.1$	(11×21)	$2\pi/20$	**–0.50285**	**–1.0395**
	(21×41)	$2\pi/40$	**–0.80388**	**–1.9488**
	(41×81)	$2\pi/80$	**–1.1049**	**–3.2217**
	Order of accuracy			**∼3.91**
$u_{\mathrm{ref}} = 0.01$	(11×21)	$2\pi/20$	**–0.50285**	**–0.4353**
	(21×41)	$2\pi/40$	**–0.80388**	**–1.5216**
	(41×81)	$2\pi/80$	**–1.1049**	**–3.1432**
	Order of accuracy			**∼4.49**
$u_{\mathrm{ref}} = 0.001$	(11×21)	$2\pi/20$	**–0.50285**	**–0.5548**
	(21×41)	$2\pi/40$	**–0.80388**	**–1.8457**
	(41×81)	$2\pi/80$	**–1.1049**	**–3.3318**
	Order of accuracy			**∼4.61**

In Table III, the efficiency of the proposed solution methodology based on the WENO finite-difference LBM is examined by comparison with the second-order finite-volume LBM in terms of the computation time with the same time step size. It is indicated that for a specified accuracy, the WENOLBM method applied requires a lower number of grid points and the computation time can be significantly reduced compared to the FVLBM. For example, the computation time of the explicit Runge-Kutta WENOLBM solver with the mesh (81×81) is about 2.5 h; however, the FVLBM requires the mesh (321×321) to give the same accuracy and the computation time is 8.0 h. It should also be noted that the computational time of the IMEX method is much less than the explicit Runge-Kutta method. The performance of the WENOLBM is improved compared to the FVLBM when considering a more accurate solution. Thus, for studying more practical problems in which high-order accuracy solutions are required to accurately represent flow physics, the performance of the WENOLBM is more emphasized compared to the FVLBM.

TABLE III. Comparison of computation time for Taylor-Green vortex problem with $\mathrm{Re} = 10\pi$ at $t = 10$ for $u_{\mathrm{ref}} = 0.001$.

		WENOLBM	FVLBM
RK4	**Grid size**	(41×41)	(81×81)
	Computation time (h)	**0.6**	**0.3**
RK4	**Grid size**	(81×81)	(321×321)
	Computation time (h)	**2.7**	**8.0**
IMEX	**Grid size**	(41×41)	(81×81)
	Computation time (h)	**0.1**	**0.1**
IMEX	**Grid size**	(81×81)	(321×321)
	Computation time (h)	**0.6**	**2.7**

Now, the accuracy of the WENOLBM is examined for the traveling Taylor vortex problem which has an advection in addition to the pure diffusion. The exact solution of the traveling Taylor vortex problem on a doubly periodic square domain $(0 \leqslant x \leqslant 2\pi,\ 0 \leqslant y \leqslant 2\pi)$ has been given in Ref. [36], and in the present simulation using the WENOLBM it is rewritten as follows:

$$
\begin{aligned}
u(x,y,t) &= u_{\mathrm{ref}}\{1 - \cos[N_1(x - u_{\mathrm{ref}}t)]\sin[N_2(y - u_{\mathrm{ref}}t)]e^{-\nu t(N_1^2+N_2^2)}\},\\
v(x,y,t) &= \frac{N_1}{N_2}u_{\mathrm{ref}}\{1 + \sin[N_1(x - u_{\mathrm{ref}}t)]\cos[N_2(y - u_{\mathrm{ref}}t)]e^{-\nu t(N_1^2+N_2^2)}\},\\
p(x,y,t) &= p_0 - \frac{1}{4}\rho_0 u_{\mathrm{ref}}^2\left[\cos[2N_1(x - u_{\mathrm{ref}}t)] + \left(\frac{N_1}{N_2}\right)^2\cos[2N_2(y - u_{\mathrm{ref}}t)]\right]e^{-2\nu t(N_1^2+N_2^2)}.
\end{aligned}
\tag{39}
$$

Note that the above relations will become the same as those given in Eq. (38) for each complete cycle. Here, the wave numbers in the x and y directions are set to be $N_1 = N_2 = 1$. The order of the accuracy of the WENOLBM applied is verified considering four computational grids, namely, (11×11), (21×21), (41×41), and (81×81) at $\mathrm{Re} = 10\pi$ and after one complete circle, i.e., at $t = 2\pi/u_{\mathrm{ref}}$. The reference velocity is set to be $u_{\mathrm{ref}} = 0.001$ and the error is calculated based on the L_2 norm of the u-velocity profile compared with the analytical solution and also that of the most refined grid (161×161). Results in Table IV show that the fifth-order accuracy is achieved for the WENOLBM even for the traveling Taylor vortex problem by considering a small value of the reference velocity (or the Mach number).

B. Doubly periodic shear layer flow

The numerical solution of the unsteady doubly periodic shear flow problem [37,38] is performed to demonstrate the stability of the high-order WENO finite-difference lattice Boltzmann method (WENOLBM) employed. This problem is an important numerical test case in order to observe whether the numerical procedure is stable when there is a strong shear in the flow domain. In this problem, the normalized velocity field is initialized as

$$
\begin{aligned}
&\frac{u}{u_0} = \begin{cases}\tanh[4(y - 1/4)/w] & y \leqslant 1/2\\ \tanh[4(3/4 - y)/w] & y > 1/2\end{cases} \qquad 0 \leqslant x \leqslant 1,\ 0 \leqslant y \leqslant 1,\\
&\frac{v}{u_0} = \delta\sin[2\pi(x + 1/4)]
\end{aligned}
\tag{40}
$$

where w approximates the initial shear layer width and δ is the strength of the initial perturbation; here, $\delta = 0.05$ and $w = 0.05$. In this problem, the shear layer between the Kelvin Helmholtz vortices rolls up due to stretching. In the present study, a (121×121) grid is used in the doubly periodic domain $0 \leqslant x,\ y \leqslant 1$ and the fluid viscosity is set to be $\upsilon = 0.0001$. The value of u_{ref} is set to be $u_{\mathrm{ref}} = 0.1$. The numerical solution of this test case is performed by implementing the WENO finite-difference LBM and the results obtained are compared

TABLE IV. Order of accuracy of the solution based on the L_2 norm of the u-velocity profile for traveling Taylor vortex problem with $\mathrm{Re} = 10\pi$ at $t = 2\pi/u_{\mathrm{ref}}$.

		Grid	Δx	$\log_{10}(\Delta x)$	$\log_{10}(L_2\,\mathrm{norm[Error]})$
$u_{\mathrm{ref}} = 0.001$	Compared with the most refined grid (161×161)	(21×21)	$2\pi/10$	**–0.2018**	**–1.7193**
		(41×41)	$2\pi/20$	**–0.5028**	**–3.1408**
		(81×81)	$2\pi/40$	**–0.8038**	**–4.6556**
		Order of accuracy			**∼4.89**
	Compared with the analytical solution	(21×21)	$2\pi/10$	**–0.2018**	**–1.7188**
		(41×41)	$2\pi/20$	**–0.5028**	**–3.1270**
		(81×81)	$2\pi/40$	**–0.8038**	**–4.6289**
		Order of accuracy			**∼4.85**

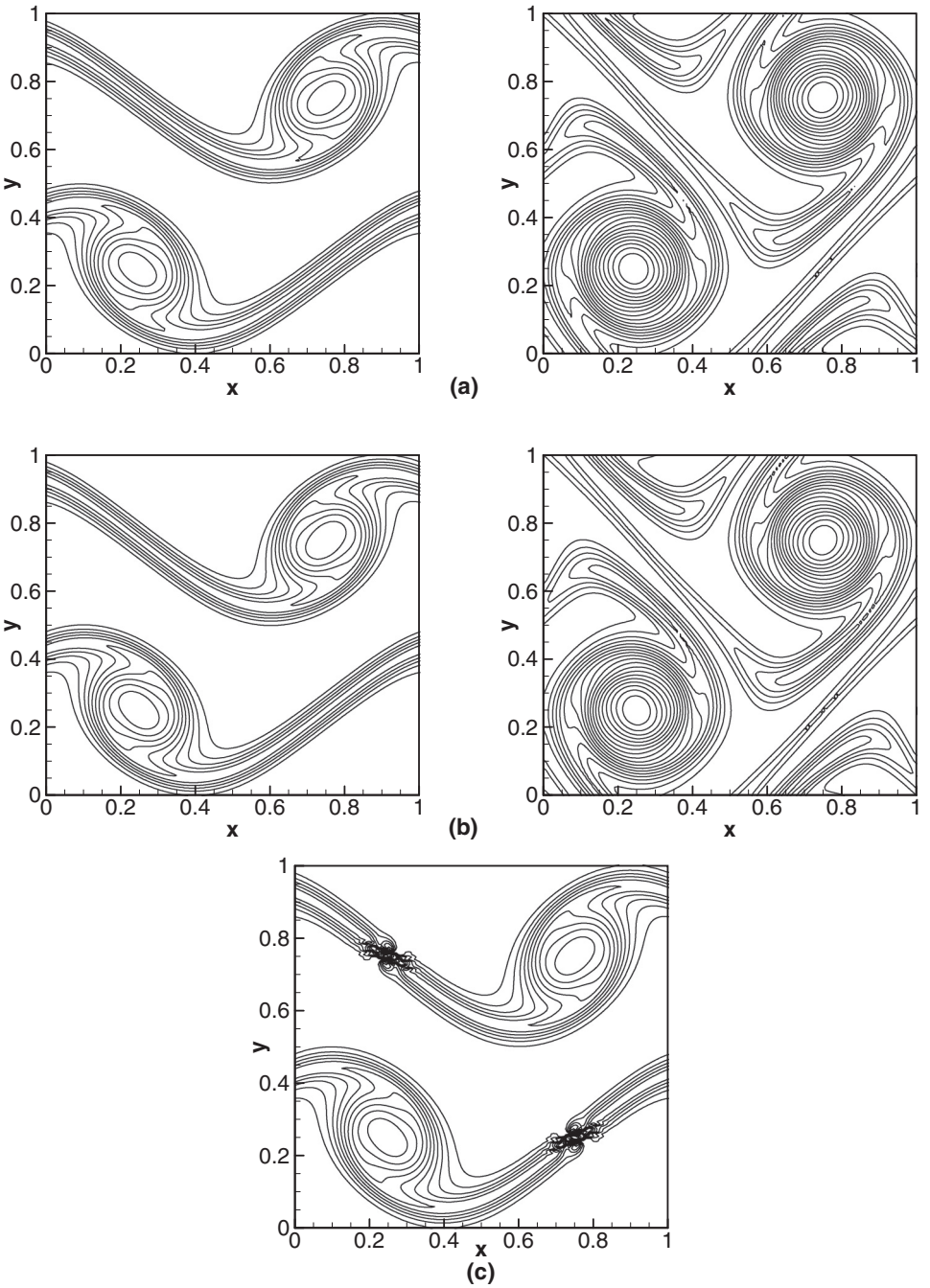

FIG. 3. Computed vorticity contours for doubly periodic shear flow at (a) $t^* = 1$, (left) $t^* = 1.5$ (right) WENOLBM; (b) $t^* = 1$ (left), $t^* = 1.5$ (right) FVLBM with numerical dissipation; and (c) $t^* = 1$ FVLBM without numerical dissipation.

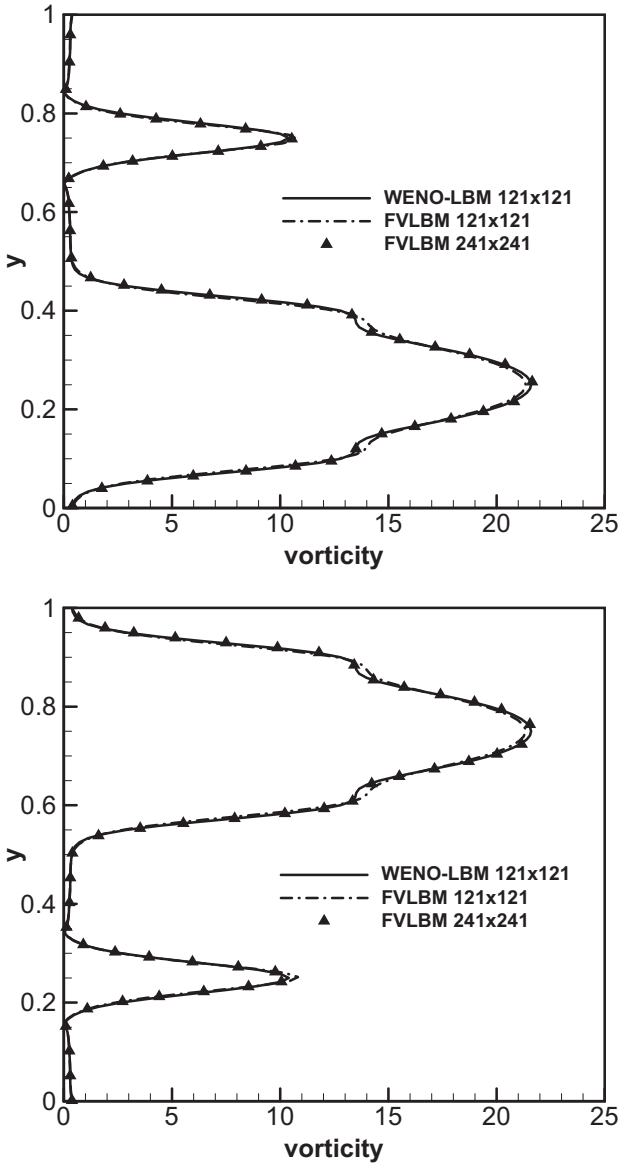

FIG. 4. Comparison of vorticity profiles at $x = 0.25$ (top) and $x = 0.75$ (bottom) for doubly periodic shear flow with $v = 0.0001$ at $t^* = 1$.

with those of the FVLBM with and without the artificial dissipation.

Figure 3 shows the vorticity contours at the nondimensional times $t^* = tu_{\text{ref}}/L = 1.0$ and $t^* = 1.5$, respectively. It is observed in the FVLBM that the solution procedure becomes unstable without the artificial dissipation, particularly at the thinnest points of the two shear layers at $t^* = 1$. As the solution marches in time towards $t^* = 1.5$, the unstable region gets larger and the solution diverges; however, the WENOLBM procedure leads to a stable solution and the roll-up of the shear layers due to the Kelvin Helmholtz vortices is accurately resolved without using any dissipation or filtering scheme. Figure 4 gives the vorticity profiles at the two sections, $x = 0.25$ and $x = 0.75$, computed by the WENOLBM compared with the FVLBM. This figure shows that the WENOLBM with the grid size (121×121) provides comparable results with the FVLBM using the grid size (241×241).

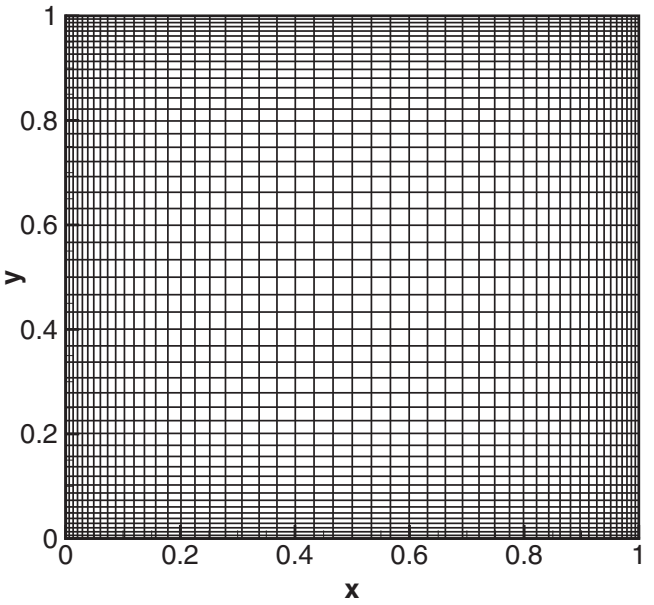

FIG. 5. A (51×51) mesh distribution for 2D cavity flow.

C. Flow in a 2D cavity

Due to its complicated flow behavior, the square lid-driven cavity is an appropriate benchmark problem to examine accuracy and stability of different numerical methods. The simple configuration of a lid-driven cavity consists of a two-dimensional square cavity in which the top wall moves with a constant velocity $u = u_{\text{ref}}$ and all the other three walls are stationary ($u = v = 0$). Since the corners in the lid-driven cavity are singular points, it is desirable to use nonuniform grids and refine the mesh near these regions to reasonably resolve the flow field there. Herein, the numerical simulations are carried out for a square cavity of height $H = 1.0$ with $u_{\text{ref}} = 0.1$ and the results are presented for three different

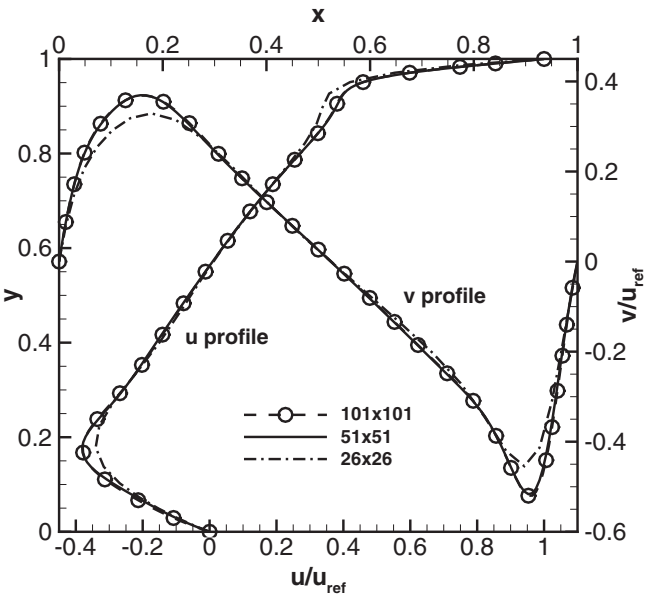

FIG. 6. Grid refinement study on velocity profiles at the midplane of 2D cavity flow with Re = 1000.

Reynolds numbers, $\mathrm{Re} = u_{\mathrm{ref}} H/v = 100$, 1000, 3200, 5000, and 7500. The nonuniform mesh used here is generated by the following transformation [39]:

$$x = y = L\frac{(2\alpha+\beta)[(\beta+1)/(\beta-1)]^{2(\eta-0.5)} + 2\alpha - \beta}{(2\alpha+1)\{1+[(\beta+1)/(\beta-1)]^{2(\eta-0.5)}\}}, \quad 0 \leqslant \eta \leqslant 1, \tag{41}$$

where β is the clustering parameter, and here it is considered to be equal to 1.1. The computational grid (51×51) is shown in Fig. 5.

A grid refinement study is performed for the flow condition $\mathrm{Re} = 1000$ to examine the sensitivity of the results obtained by applying the WENOLBM to the grid size. Three different grids $(I_{\max}, J_{\max}) = (26,26)$, $(51,51)$, $(101,101)$ are used and

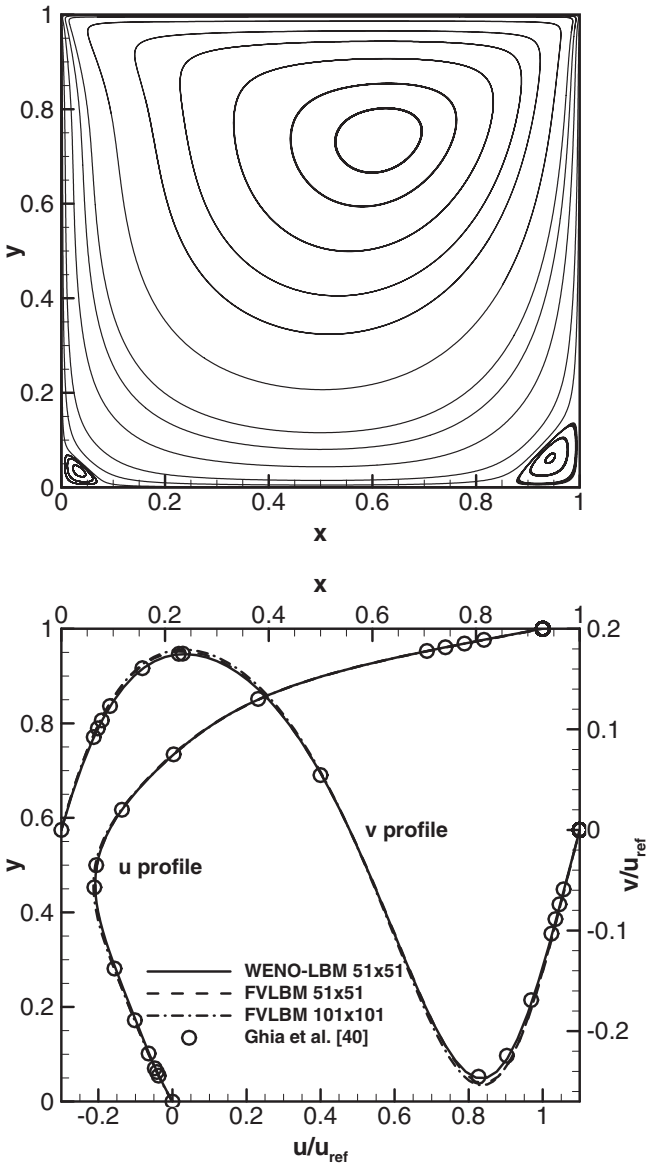

FIG. 7. Computed flow field shown by streamlines (top) and comparison of velocity profiles (bottom) for 2D cavity flow with $\mathrm{Re} = 100$.

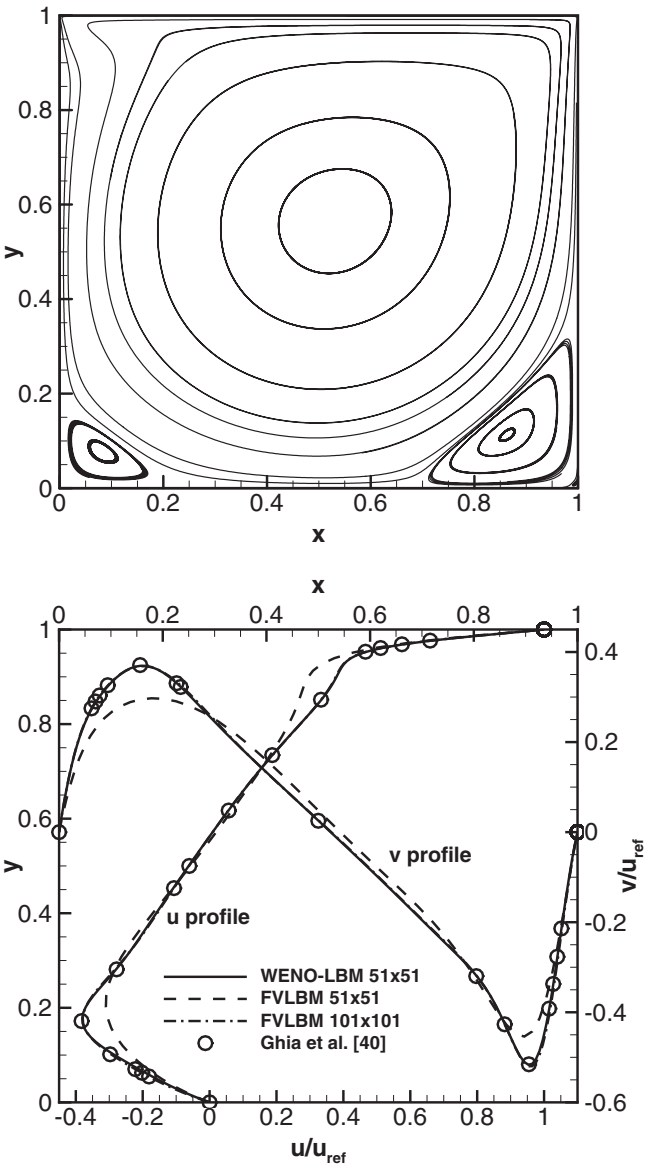

FIG. 8. Computed flow field shown by streamlines (top) and comparison of velocity profiles (bottom) for 2D cavity flow with $\mathrm{Re} = 1000$.

both the u-velocity profile along the vertical center line and the v-velocity profile along the horizontal center line are plotted in Fig. 6 for these grids. The sensitivity study has shown that for $\mathrm{Re} = 100$, 1000, and 3200 the grid (51×51), and for $\mathrm{Re} = 5000$ and 7500 the grid (101×101), are appropriate ones for an accurate calculation of the flow field by applying the WENOLBM on the nonuniform grids.

Figures 7–11 give the computed flow field shown by the streamlines and also comparisons of the velocity profiles in the midplanes for the mentioned Reynolds numbers. The effect of the value of Reynolds number on the flow structure and the velocity profiles is observed clearly in these figures. For flows with $\mathrm{Re} = 100$ and 1000, three vortices appear in the cavity: a primary one at the center and a pair of secondary ones in the lower corners of the cavity. It is indicated that by increasing the value of Re, the flow structure becomes more complex and

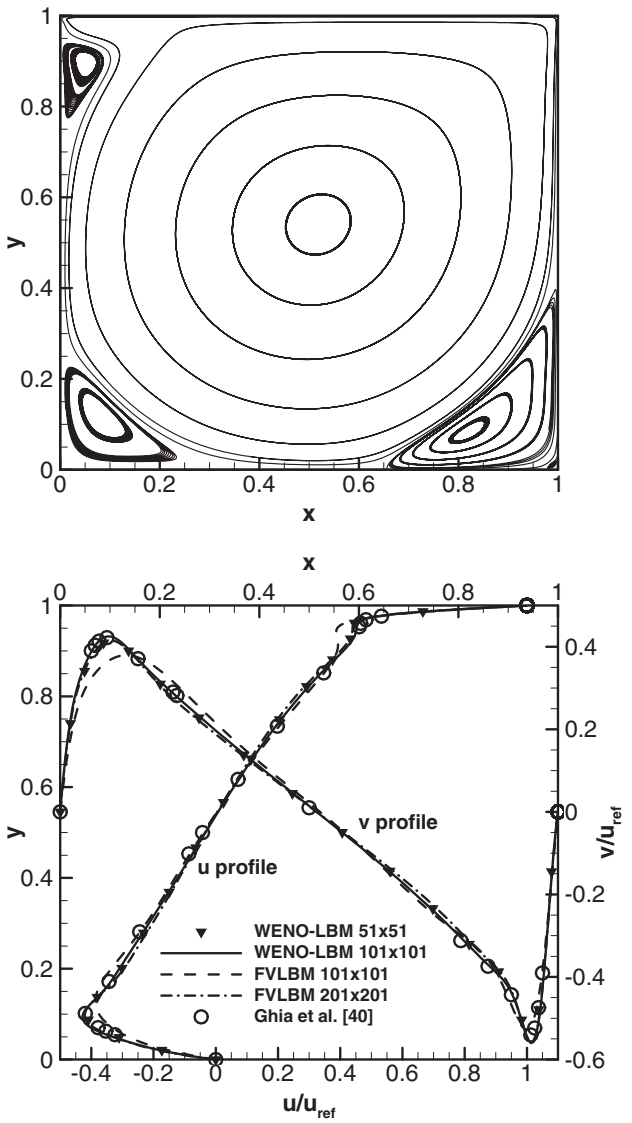

FIG. 9. Computed flow field shown by streamlines (top) and comparison of velocity profiles (bottom) for 2D cavity flow with Re = 3200.

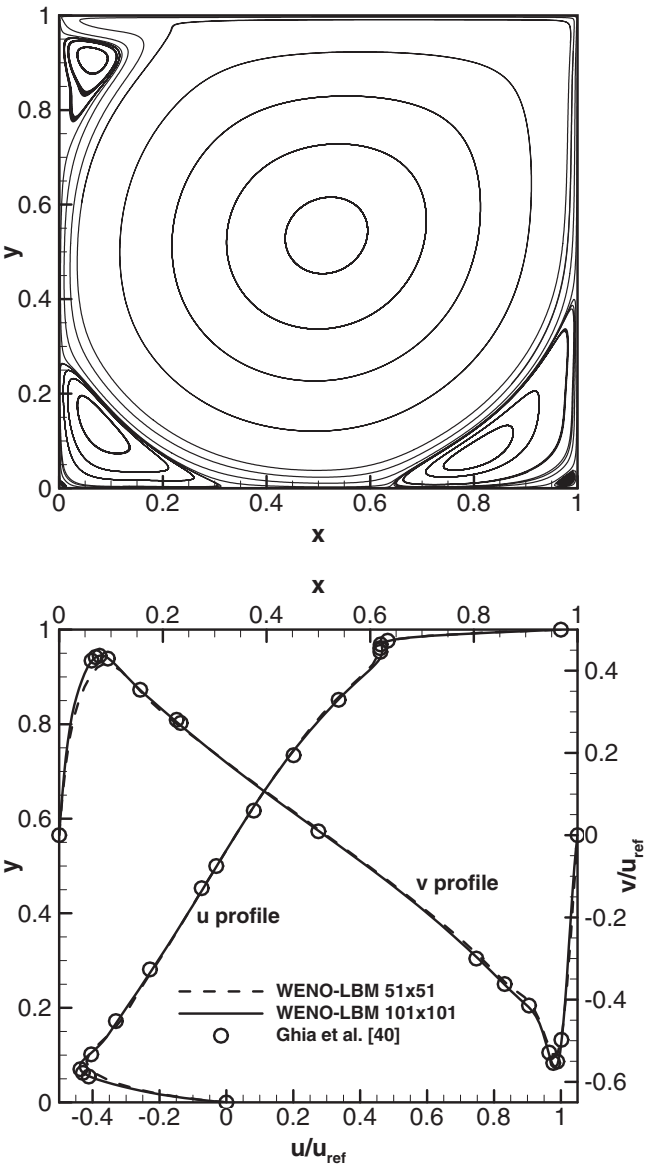

FIG. 10. Computed flow field shown by streamlines (top) and comparison of velocity profiles (bottom) for 2D cavity flow with Re = 5000.

for higher Re, other recirculating regions are formed near the upper left corner and the lower left and right corners, and they are well resolved by applying the WENOLBM.

The study shows that the flow structure is reasonably resolved by the high-order WENO finite-difference LBM implemented on the nonuniform grids. The present results obtained by applying the fifth-order WENO finite-difference LBM (WENOLBM) on the relatively coarse meshes are compared with the benchmark results by Ghia *et al.* [40] for this steady test case for different Reynolds numbers which exhibit excellent agreement. It is found that the present solution procedure based on the WENOLBM allows the calculation of the flow field accurately with a smaller number of grid points compared with the second-order finite-volume lattice Boltzmann (FVLBM). Note that the performance of the WENOLBM is improved and highlighted compared to the FVLBM by increasing Re.

To assess the efficiency of the WENOLBM compared to the FVLBM, the computation time of these two LBM solvers to obtain the steady-state solution for Re = 3200 using different grid sizes is given in Table V. The convergence history of the solution based on the error calculated by the L_∞ norm (maximum norm) of the u-velocity profile in the flow field at this Reynolds number for the IMEX scheme is shown in Fig. 12. It is observed that the WENOLBM has a faster convergence rate than the FVLBM to reach the steady-state solution. As indicated in Fig. 9, the results obtained by the WENOLBM with the mesh (51×51) are comparable with that of the FVLBM with the mesh (201×201) and Table V indicates that the computation time of the steady-state solution obtained by applying the WENOLBM is much less than that of the FVLBM. Note also that the maximum time step size of the implicit-explicit scheme (IMEX) is higher than

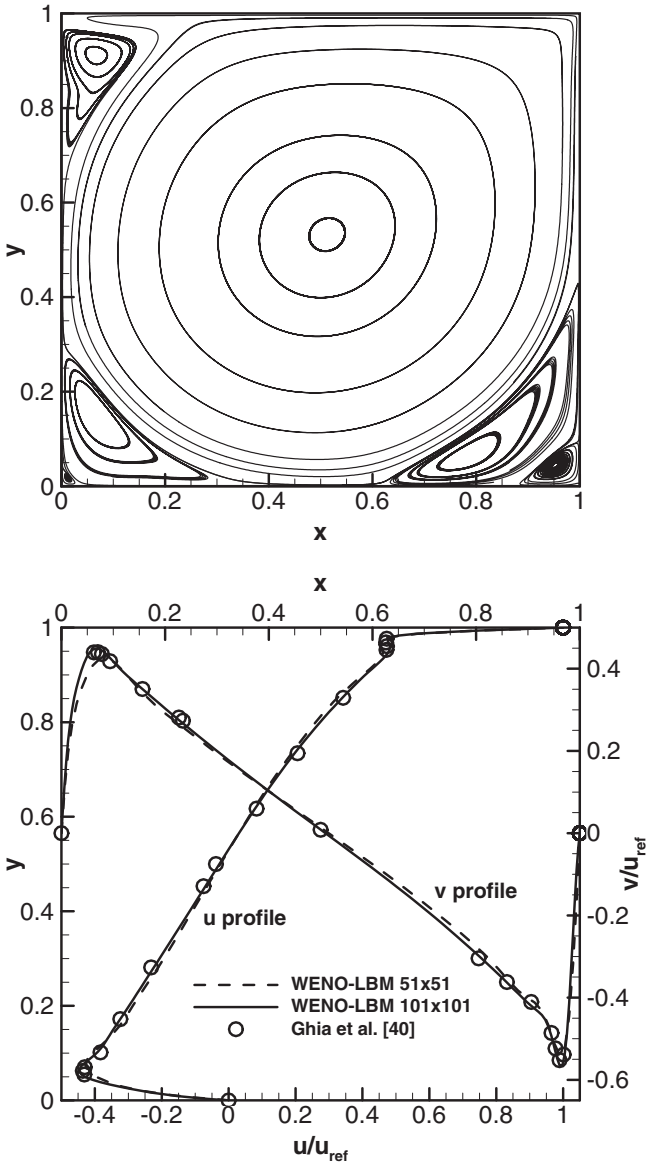

FIG. 11. Computed flow field shown by streamlines (top) and comparison of velocity profiles (bottom) for 2D cavity flow with Re = 7500.

that of the explicit Runge-Kutta scheme (RK4) and therefore the computation time of the IMEX scheme to reach the steady-state solution is much less than that of the RK4 method.

TABLE V. Comparison of computation time for 2D cavity flow with Re = 3200.

		WENOLBM	FVLBM
RK4	**Grid size**	(51 × 51)	(101 × 101)
	Computation time (h)	**20.9**	**22.1**
RK4	**Grid size**	(101 × 101)	(201 × 201)
	Computation time (h)	**130.7**	**151.2**
IMEX	**Grid size**	(51 × 51)	(101 × 101)
	Computation time (h)	**1.0**	**1.1**
IMEX	**Grid size**	(101 × 101)	(201 × 201)
	Computation time (h)	**6.9**	**8.8**

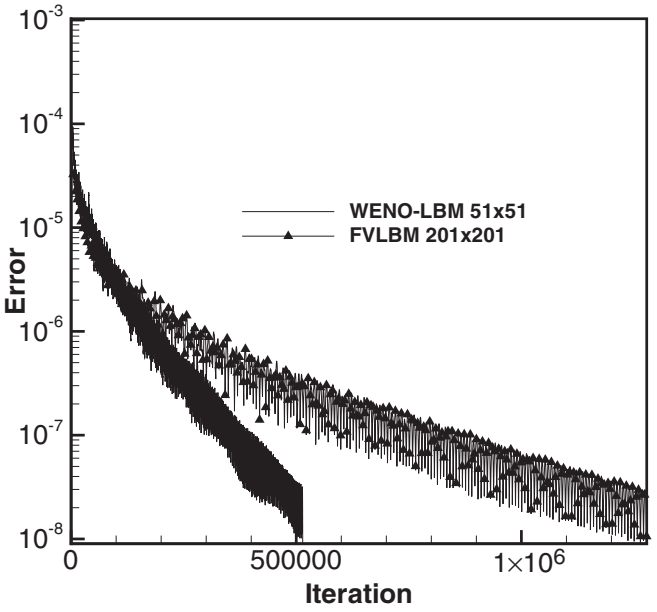

FIG. 12. Comparison of L_2-norm error of u-velocity profile for 2D cavity flow with Re = 3200.

To compare the numerical stability of the explicit Runge-Kutta method (RK4) and the implicit-explicit Runge-Kutta scheme (IMEX), the stability regions of each scheme based on $\Delta t/\tau$ and CFL $= \Delta t/\Delta x$ are presented for different Reynolds numbers. Broadly speaking, $\Delta t/\tau$ represents the nonlinear stability constraint imposed by the collision and the CFL number represents the linear stability constraint of the explicit advection [28]. In all the plots, • indicates a stable solution while ○ indicates an unstable solution. Figure 13 shows the stability region of the RK4 and IMEX schemes for Re = 100 obtained by the present solution by applying the WENOLBM. We observe that the RK4 scheme is unstable beyond $\Delta t/\tau > 2$ and the stable solutions for $\Delta t/\tau < 2$ are obtained only at small CFL numbers. The IMEX scheme gives a stable solution for higher $\Delta t/\tau$ and the CFL number compared to the RK4 scheme. As Reynolds number increases, the collision term becomes more stiff and the benefit of using the IMEX scheme becomes more noticeable. For example, in Fig. 13, the stability regions of the RK4 and IMEX schemes for Re = 1000 and Re = 3200 are presented. It is evident that with increasing the Reynolds number the stability region of the IMEX scheme becomes wider.

D. Cylindrical Couette flow

To investigate the accuracy of the WENOLBM in the generalized curvilinear coordinates, the cylindrical Couette flow between the two cylinders of radius r_1 and r_2 is simulated here. In this problem, the outer cylinder is stationary and the inner cylinder moves with the constant angular velocity u_θ. Here, $r_1 = 4$, $r_2 = 8$, $u_\theta = u_{\text{ref}}$, and $\text{Re} = u_{\text{ref}} r_1/\nu = 50$. Note that the exact solution for the steady cylindrical Couette flow does not depend on the Reynolds number and the steady angular velocity is given as

$$\frac{u_\theta(r)}{u_{\text{ref}}} = \left(\frac{r_2}{r_1} - \frac{r_1}{r_2}\right)^{-1}\left(\frac{r_2}{r} - \frac{r}{r_2}\right). \tag{42}$$

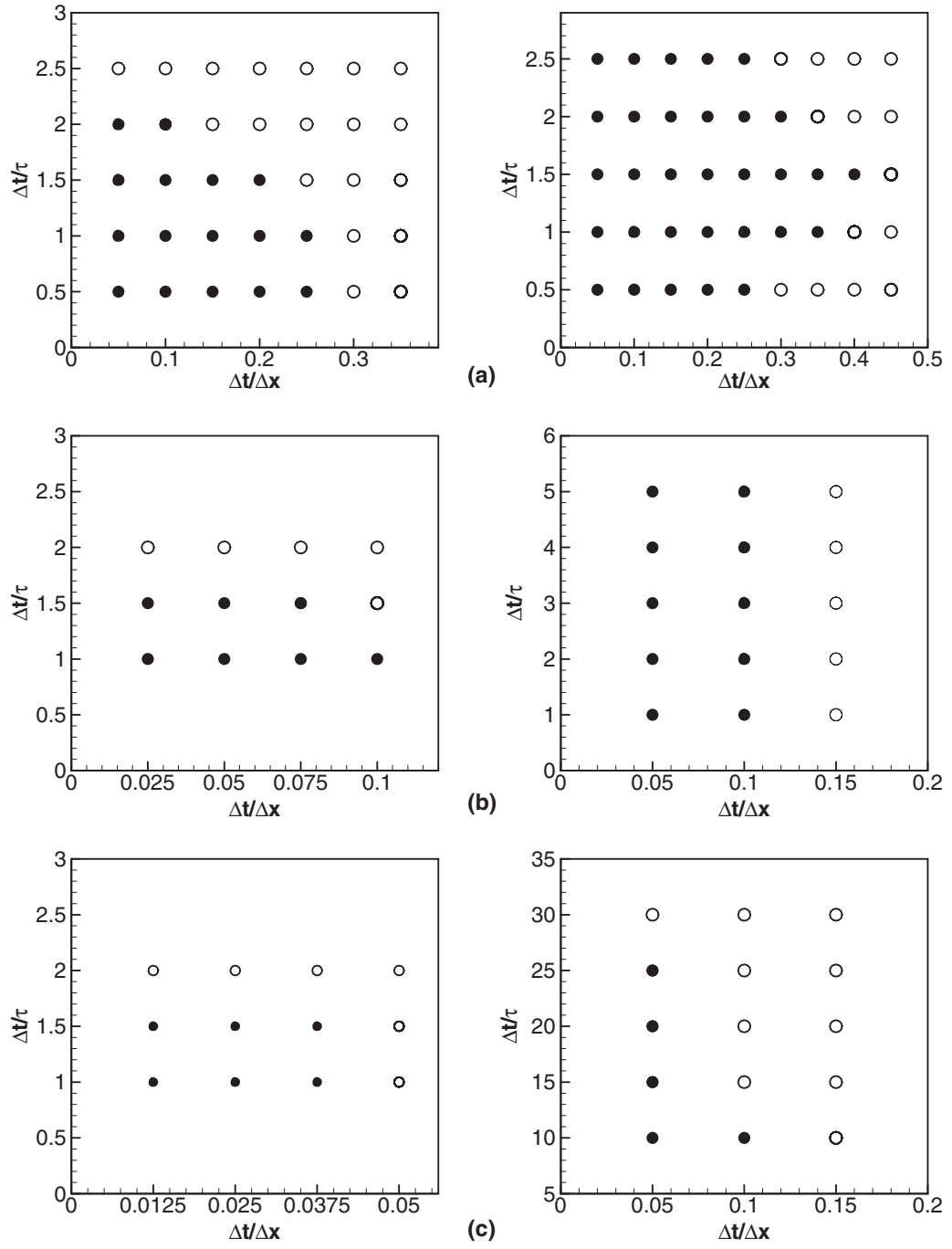

FIG. 13. Stability region of the RK4 (left) and IMEX (right) schemes for (a) Re = 100, (b) Re = 1000, (c) Re = 3200.

Figure 14 represents the computational grid (21 × 21) used to simulate this problem. Figure 15 gives the computed flow field shown by the velocity vectors and Fig. 16 shows the comparison of the steady angular velocity profile computed by the WENOLBM with the exact solution which indicates excellent agreement. It should be noted that this problem has been simulated by Tiwari and Vanka [41] by applying the ghost fluid LBM (GF LBM) and thus the accuracy of the present solution based on the WENOLBM can be assessed by comparison with their solution based on the standard interpolation bounce back LBM. They have solved the cylindrical Couette flow with $u_{\text{ref}} = 0.057$ (corresponds to the Mach number $M = 0.1$) using grid sizes (41 × 41), (81 × 81), and (161 × 161) grid points and they have reported the L_2-norm error of the steady angular velocity for these grids compared with the solution of the most refined grid (321 × 321). The calculations are performed for the WENOLBM with three grid sizes (11 × 11), (21 × 21), and (41 × 41), and the error for each grid is calculated based on the L_2 norm of the steady angular velocity profile compared with the solution of the most refined grid (81 × 81) obtained by the WENOLBM. Figure 17 indicates that the WENOLBM provides a more accurate solution than the GF LBM by considering the same number of grid points. Note that in the GF LBM (or the

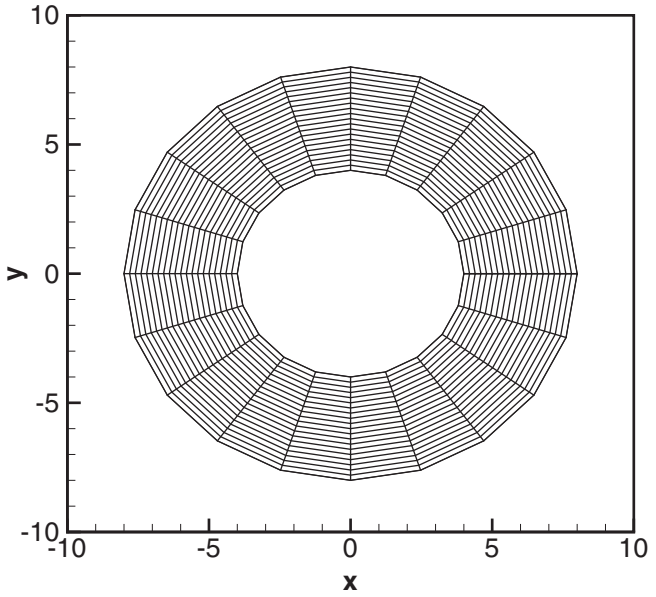

FIG. 14. A (21 × 21) mesh distribution for cylindrical Couette flow.

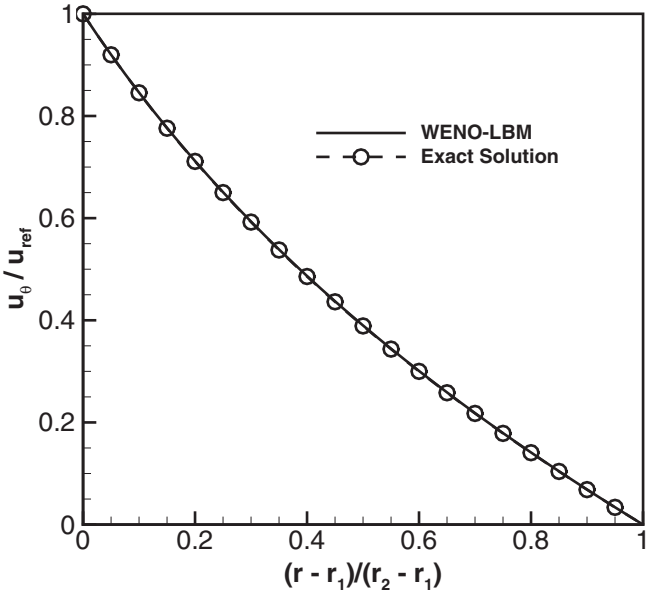

FIG. 16. Comparison of steady angular velocity profile for cylindrical Couette flow with Re = 50.

interpolation bounce back LBM) [41], the geometry is covered by a Cartesian grid and therefore some grid points are not located in the solution domain and this procedure causes a larger error compared to the WENOLBM implemented in the curvilinear coordinates. Note also that the slope of the error for the WENOLBM is about 5 which is higher than that of the GF LBM which is about 2. The calculations are also carried out for a smaller reference velocity, i.e., $u_{ref} = 0.01$ and the order of the accuracy of the WENOLBM is obtained for this condition. The error is calculated based on the L_2 norm of the steady angular velocity profile compared with the exact solution and also the solution of the most refined grid (81 × 81) by applying the WENOLBM. Results in Table VI show that the order of the accuracy of the WENOLBM applied is 4.51 for $u_{ref} = 0.01$ by comparing with the exact solution. It is also indicated that the fifth-order accuracy of the WENOLBM is achieved when the error is calculated based on the solution of the most refined grid.

E. Flow over a 2D circular cylinder

Although the flow in the square cavity is complex, the geometry is nevertheless simple because only flat boundaries are involved. To demonstrate the capability of the present solution procedure for the numerical simulation of the fluid

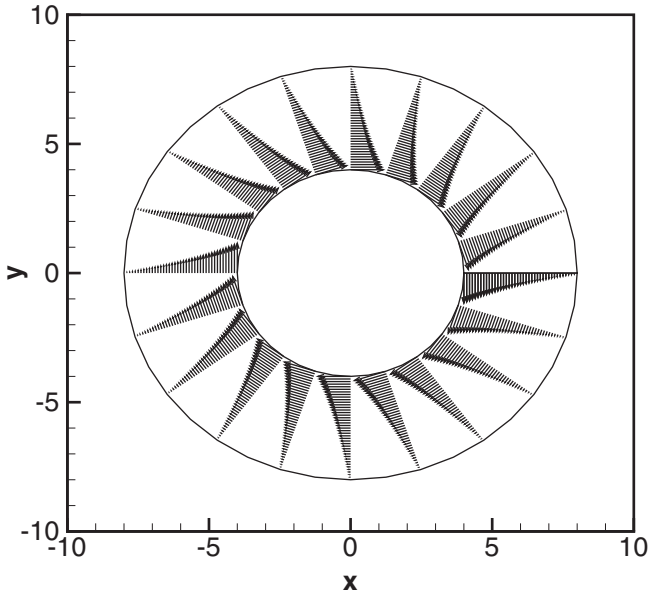

FIG. 15. Computed flow field shown by velocity vectors for cylindrical Couette flow with Re = 50.

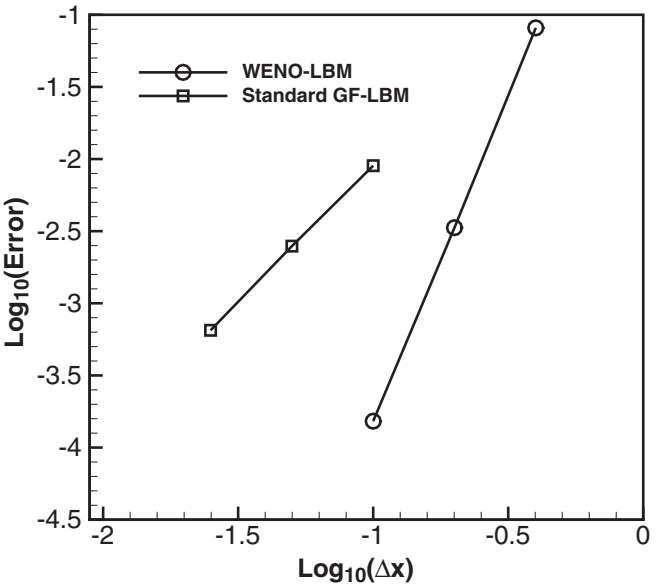

FIG. 17. Comparison of L_2-norm error of the solution for cylindrical Couette flow problem with Re = 50 and $u_{ref} = 0.057$.

TABLE VI. Order of accuracy of the solution based on the L_2 norm of steady angular velocity profile for cylindrical Couette flow problem with Re = 50.

		Grid	Δr	$\log_{10}(\Delta r)$	$\log_{10}(L_2$ norm[Error])
$u_{\text{ref}} = 0.01$	Compared with the most refined grid (81 × 81)	(11 × 11)	4/10	**–0.3010**	**–0.7205**
		(21 × 21)	4/20	**–0.6020**	**–1.9931**
		(41 × 41)	4/40	**–0.9030**	**–3.7013**
		Order of accuracy			**∼4.96**
	Compared with the analytical solution	(11 × 11)	4/10	**–0.3010**	**–0.7217**
		(21 × 21)	4/20	**–0.6020**	**–2.031**
		(41 × 41)	4/40	**–0.9030**	**–3.4291**
		Order of accuracy			**∼4.51**

flow with curved boundaries, the two-dimensional steady flow over a circular cylinder is studied at different Reynolds numbers $\text{Re} = u_{\text{ref}} D/\upsilon$, where D is the diameter of the cylinder and the free stream velocity u_{ref} is considered 0.1 in all the simulations.

This problem has been studied extensively as a benchmark test case by many researchers and thus there are numerous experimental and numerical results available in the literature for this test case for the validation of the results obtained by applying the WENO finite-difference LBM in the generalized curvilinear coordinates. For Reynolds numbers lower than its critical value ($\text{Re}_{\text{cr}} \approx 47$), a steady-state condition is obtained and a pair of recirculating regions appears behind the cylinder. Herein, the computations are performed for Re = 10, 20, and 40, and the results are compared with the numerical and experimental results.

For this test case, an O-type grid with the size of (101 × 51) is used. The diameter of the cylinder is equal to unity and the outer radius of the computational domain is set to be 30 times the diameter of the cylinder. The mesh is stretched in the ξ direction near the rear stagnation point. For the stretching in the η direction, which is in the wall-normal direction here, the

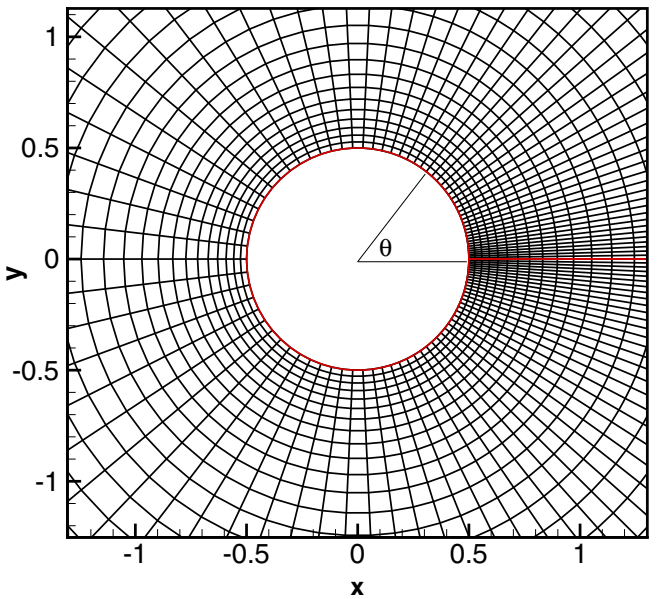

FIG. 18. A (101 × 51) mesh distribution around the circular cylinder.

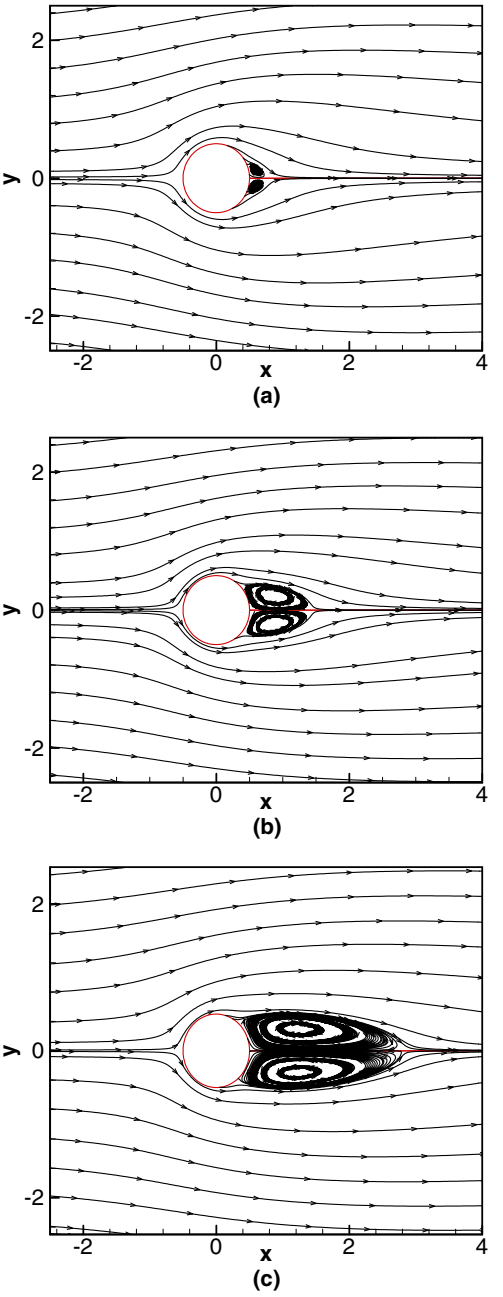

FIG. 19. Computed flow field for steady flow over the circular cylinder shown by streamlines with (a) Re = 10, (b) Re = 20, and (c) Re = 40.

TABLE VII. Comparison of the results of steady flow over the circular cylinder with the available results.

Re	Author(s)	Method	C_d	$-C_p(0)$	$C_p(\pi)$	$2\frac{L}{D}$	θ_s
10	Coutanceau and Bouard [42]	Experiment	–	–	–	–	32.5
	Tritton [43]	Experiment	3.06	–	–	0.68	–
	Dennis and Chang [44]	Navier-Stokes	2.846	0.742	1.489	0.53	29.6
	Nieuwstadt and Keller [45]	Navier-Stokes	2.828	0.692	1.500	0.434	27.96
	Guo and Zhao [9]	FDLBM	3.049	0.661	1.476	0.486	28.13
	Mei and Shyy [7]	FDLBM	–	–	–	0.489	30.0
	He *et al.* [46]	IS LBM	3.170	0.687	1.393	0.474	26.89
	Imamura *et al.* [47]	GI LBM	2.848	0.733	1.403	0.478	26.0
	Hejranfar and Ezzatneshan [15]	CFDLBM	2.801	0.6733	1.4867	0.489	29.83
	Present solution	WENOLBM	2.813	0.673	1.468	0.488	29.86
		FVLBM	–	–	–	–	–
20	Coutanceau and Bouard [42]	Experiment	–	–	–	1.86	44.8
	Tritton [43]	Experiment	2.2	–	–	–	–
	Dennis and Chang [44]	Navier-Stokes	2.045	0.589	1.269	1.88	43.7
	Nieuwstadt and Keller [45]	Navier-Stokes	2.053	0.582	1.274	1.786	43.37
	Guo and Zhao [9]	FDLBM	2.048	0.512	1.289	1.824	43.59
	Mei and Shyy [7]	FDLBM	–	–	–	1.804	42.1
	He *et al.* [46]	IS LBM	2.152	0.567	1.233	1.842	42.96
	Imamura *et al.* [47]	GI LBM	2.051	0.589	1.251	1.852	43.3
	Hejranfar and Ezzatneshan [15]	CFDLBM	2.021	0.5465	1.2659	1.848	43.58
	Present solution	WENOLBM	2.062	0.565	1.281	1.80	43.94
		FVLBM	–	–	–	–	–
40	Coutanceau and Bouard [42]	Experiment	–	–	–	4.26	53.5
	Tritton [43]	Experiment	1.65	–	–	–	–
	Dennis and Chang [44]	Navier-Stokes	1.522	0.509	1.144	4.69	53.8
	Nieuwstadt and Keller [45]	Navier-Stokes	1.550	0.554	1.117	4.357	53.34
	Guo and Zhao [9]	FDLBM	1.475	0.448	1.168	4.168	52.44
	Mei and Shyy [7]	FDLBM	–	–	–	4.38	50.12
	He *et al.* [46]	IS LBM	1.499	0.487	1.113	4.490	52.84
	Imamura *et al.* [47]	GI LBM	1.538	0.514	1.156	4.454	52.4
	Hejranfar and Ezzatneshan [15]	CFDLBM	1.515	0.4808	1.154	4.510	51.86
	Present solution	WENOLBM	1.524	0.476	1.158	4.568	53.29
		FVLBM	1.518	0.485	1.129	4.548	54.39

following transformation function is used:

$$y_n = \delta \frac{(\beta+1)-(\beta-1)[(\beta+1)/(\beta-1)]^{(1-\eta)}}{1+[(\beta+1)/(\beta-1)]^{(1-\eta)}}, \quad 0 \leqslant \eta \leqslant 1, \tag{43}$$

where δ is the radial distance between the body and the outer boundary. The stretching parameter β is set to be 1.06 for all the cases computed. The mesh near the body surface is shown in Fig. 18.

Figure 19 shows the streamlines for the computed flow field for Re = 10,20, and 40 and a pair of stationary recirculating regions appears in the wake of the cylinder for each condition. It is observed that the length of the recirculating region L and the separation angle θ_s increase as the Reynolds number increases. In Table VII, the computed results, namely, the hydrodynamic coefficients and the location of separation and reattachment points for different Reynolds numbers are compared with the available experimental and numerical results. As shown in this table, the present results obtained by applying the WENO finite-difference LBM are compared well with the results of the other studies [7,9,42–48]. Figures 20 and 21 show the distribution of the surface pressure coefficient

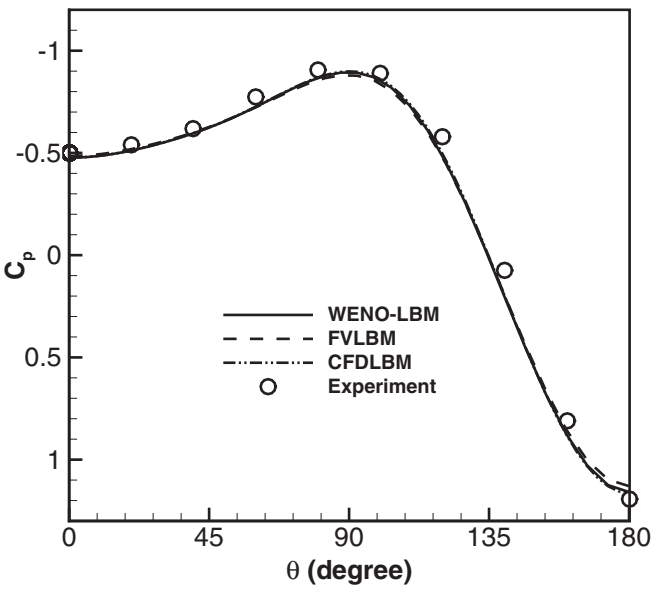

FIG. 20. Comparison of surface pressure coefficient distribution for the circular cylinder with Re = 40.

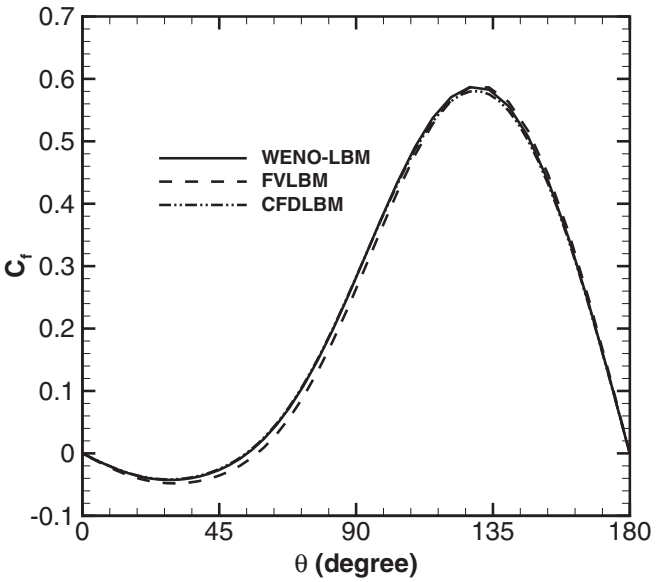

FIG. 21. Comparison of skin friction coefficient distribution for the circular cylinder with Re = 40.

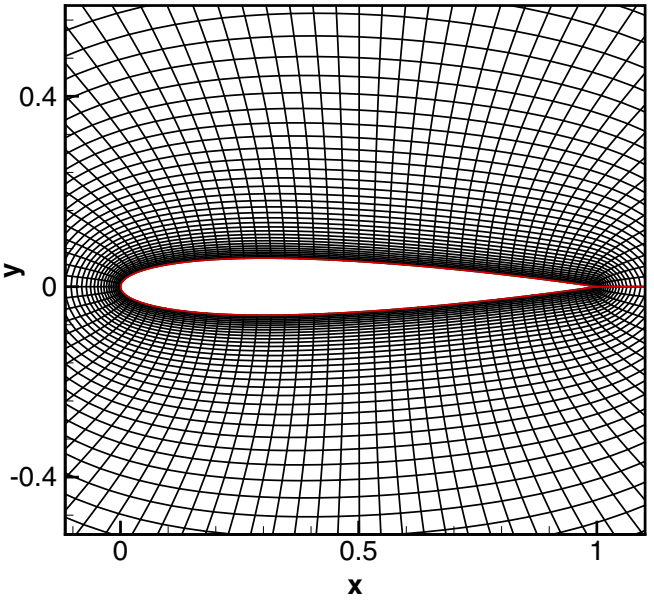

FIG. 22. A (101 × 71) mesh distribution around the NACA0012 hydrofoil.

and the skin friction coefficient obtained by employing the WENO finite-difference LBM (WENOLBM) in comparison with the experimental data [48], the fourth-order compact finite-difference LBM (CFDLBM) [16], and the second-order finite-volume LBM (FVLBM) for the Reynolds number 40, which exhibits good agreement.

F. Flow around the NACA0012 hydrofoil

The steady and unsteady laminar flows around the NACA0012 hydrofoil are simulated to demonstrate the accuracy and robustness of the present solution methodology based on the WENO finite-difference LBM in the generalized curvilinear coordinates. In the present work, the steady-state solutions are studied at Re = 500 and two angles of attack $\alpha = 0^\circ$ and 10°. Here, the Reynolds number $\mathrm{Re} = u_{\mathrm{ref}} c/\upsilon$ is defined based on the free stream velocity $u_{\mathrm{ref}} = 0.1$ and the chord length of the hydrofoil $c = 1$. The grid lines are nearly orthogonal to the body surface with an appropriate clustering for accurately resolving the flow field near the body surface. Figure 22 shows the (101 × 71) mesh system near the hydrofoil geometry employed for these simulations. For this geometry, the radius of the computational domain is set to be 10 chords. A grid refinement study is performed based on three grid systems, the coarse grid (61 × 41), the medium grid (101 × 71), and the fine grid (201 × 121). As shown in Fig. 23, the differences between the predicted surface pressure coefficient distributions for the medium and fine meshes are negligible and the solution is independent of the grid size. Therefore, the medium grid system is chosen for all the subsequent simulations, because it needs less computational effort without affecting the accuracy of the solution.

The pressure contours and the streamlines obtained by the present solution for the flow around the NACA0012 hydrofoil with Re = 500 at the angles of attack $\alpha = 0^\circ$ and 10° are shown in Fig. 24. A symmetry flow pattern is observed at $\alpha = 0^\circ$, while the flow separation occurs in the suction side of the hydrofoil at $\alpha = 10^\circ$. Figures 25 and 26 compare the computed results by the implementation of the WENO finite-difference LBM in the curvilinear coordinates with the results of the second-order finite-volume LBM, the fourth-order compact finite-difference LBM (CFDLBM) [16], and the interacting boundary layer solution by Hafez *et al.* [49]. The present study shows that the implemented algorithm can obtain accurate and reliable results for this geometry at relatively high angles of attack. In Figs. 27 and 28, the surface pressure coefficient distribution and the velocity profiles at $x/c = 0.5$ calculated based on the WENO finite-difference LBM are compared with the results of the generalized form of interpolation

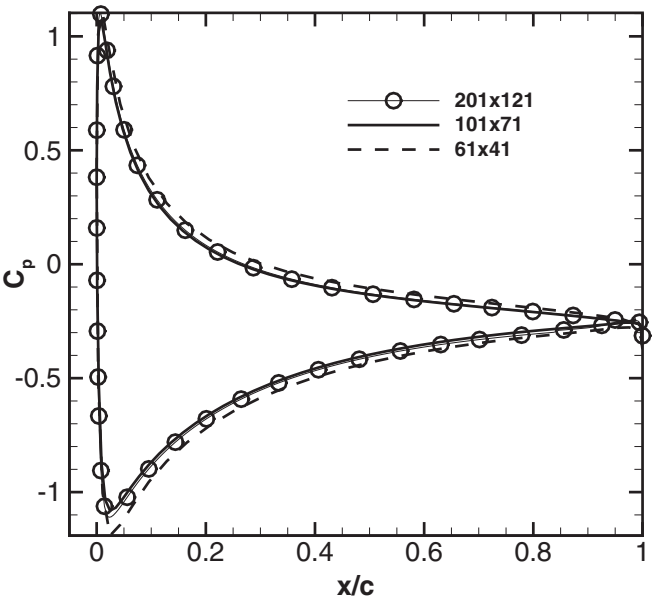

FIG. 23. Grid refinement study on surface pressure coefficient distribution of the NACA0012 hydrofoil with Re = 500 and $\alpha = 10^\circ$.

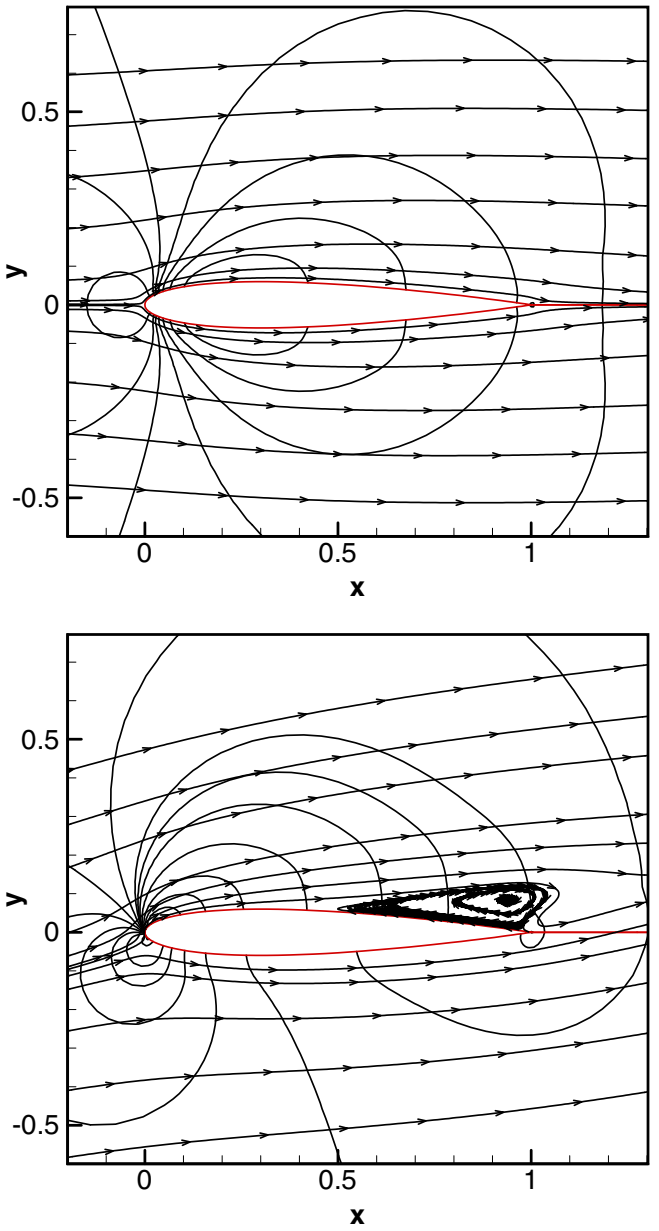

FIG. 24. Computed flow field around the NACA0012 hydrofoil shown by pressure contours and streamlines with Re = 500 and $\alpha = 0^\circ$ (top) and $\alpha = 10^\circ$ (bottom).

supplemented LBM (GI LBM) code by Imamura *et al.* [50] at Re = 500 and $\alpha = 0^\circ$. As shown in this figure, the results obtained are in good agreement with these LBM solvers which implies the validity of the WENO finite-difference LBM applied.

To demonstrate the capability of the presented method to resolve time-dependent flows with curve geometries, the numerical solution of the unsteady laminar flow over the NACA0012 hydrofoil at the Reynolds number Re = 800 and the angle of attack $\alpha = 20^\circ$ is also performed. At this condition, the flow over the hydrofoil becomes periodically unsteady with the development of a vortex street. Here, the computations are performed with the grid size of (126×121) and the radius of the computational domain is set to be

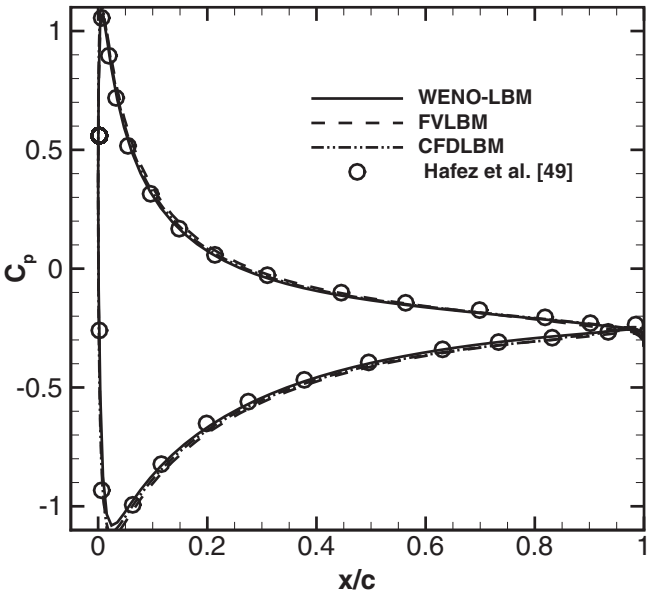

FIG. 25. Comparison of surface pressure coefficient distribution for the NACA0012 hydrofoil with Re = 500 and $\alpha = 10^\circ$.

20 chords. Figure 29 shows the instantaneous streamlines around the hydrofoil at two different dimensionless times. The low-frequency periodical vortex shedding is clearly observed in this figure. The temporal development of the v-velocity component at the point $(x/c, y/c) = (1.1, 0.0)$ behind the NACA0012 hydrofoil calculated based on the present solution procedure is given in Fig. 30 and compared with those of the fourth-order compact finite-difference LBM (CFDLBM) [16] and Hafez *et al.* [49], which are almost identical, and the small differences observed between these solution procedures may be due to different numerical algorithms with different accuracies or different grid sizes or distributions used.

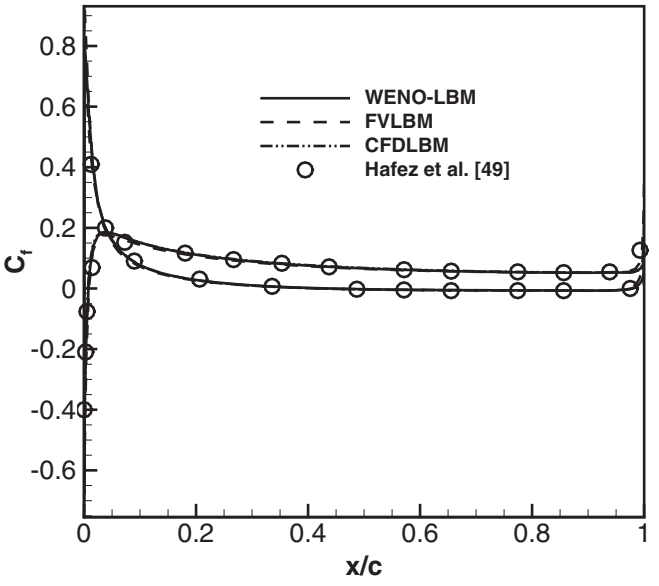

FIG. 26. Comparison of skin friction coefficient distribution for the NACA0012 hydrofoil with Re = 500 and $\alpha = 10^\circ$.

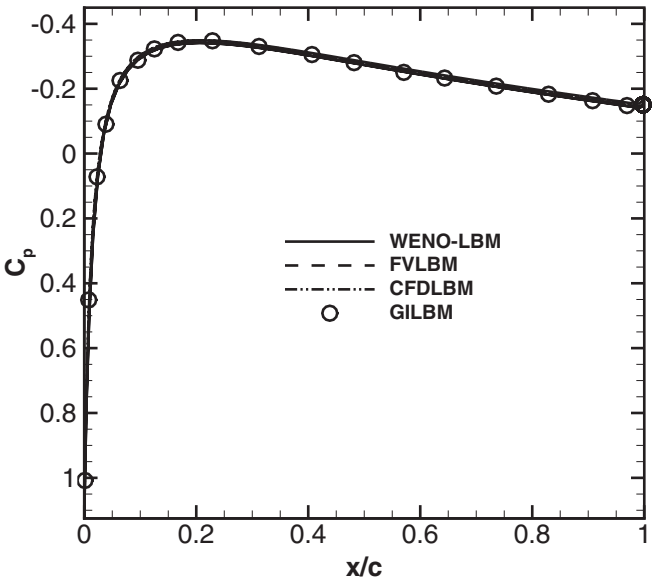

FIG. 27. Comparison of surface pressure coefficient distribution for the NACA0012 hydrofoil with Re = 500 and $\alpha = 0^\circ$.

VII. EXTENSION OF THE METHODOLOGY TO THREE DIMENSIONS

The formulation of the WENOLBM can be straightforwardly extended to three dimensions, and here a brief description is given for the 3D formulation. In 3D, the lattice Boltzmann equation (LBE) with the BGK approximation of the collision term can be written as

$$\frac{\partial f_\alpha}{\partial t} + e_\alpha \cdot \nabla f_\alpha = -\frac{1}{\tau}\left(f_\alpha - f_\alpha^{\mathrm{eq}}\right), \quad \alpha = 0,1,\ldots,18, \tag{44}$$

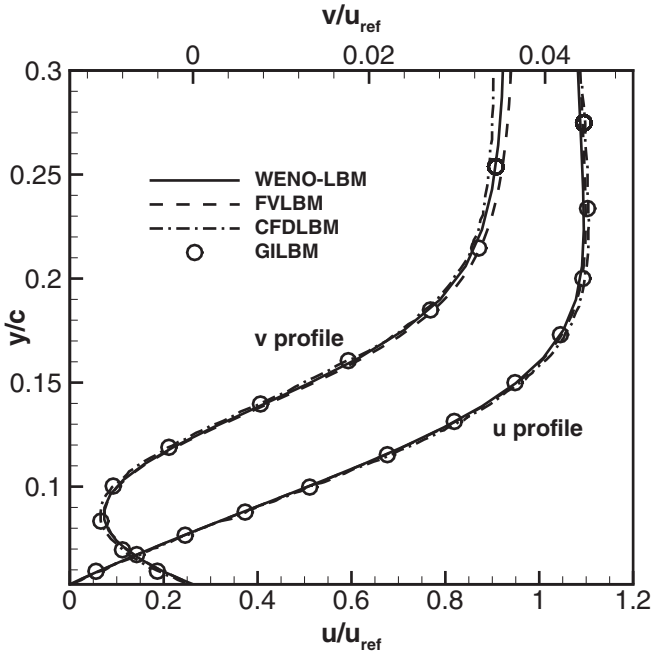

FIG. 28. Comparison of boundary layer profile for the NACA0012 hydrofoil with Re = 500 and $\alpha = 0^\circ$ at $x/c = 0.5$.

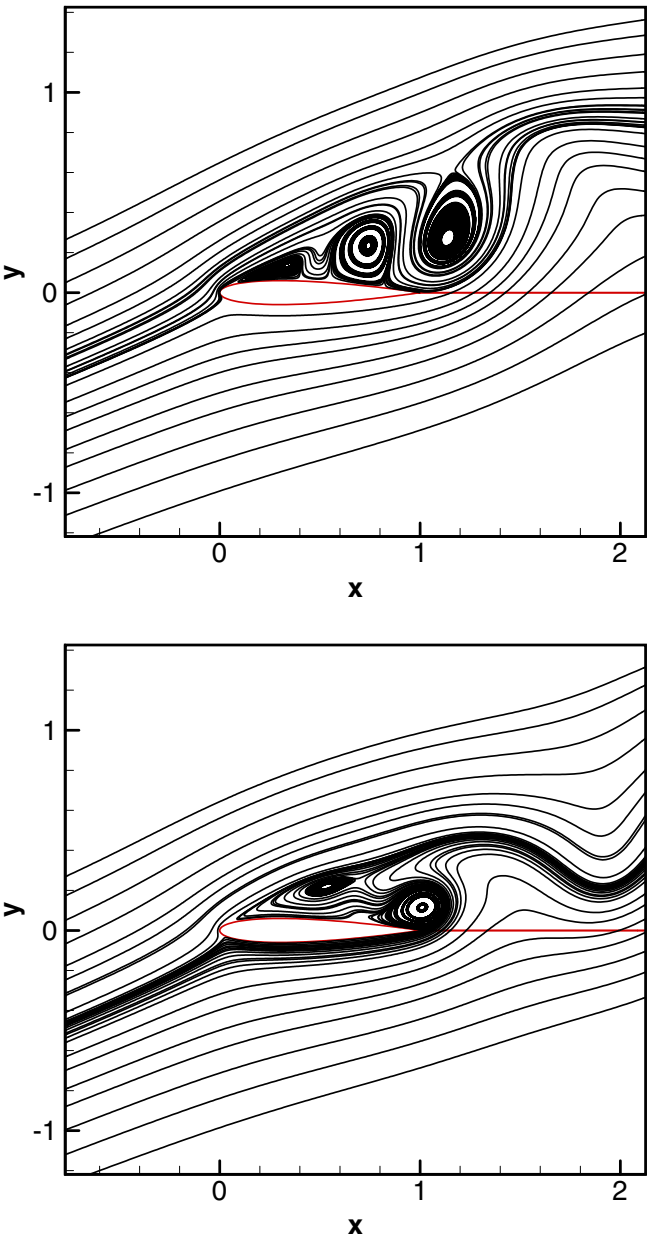

FIG. 29. Computed flow field for unsteady periodic flow over the NACA0012 hydrofoil shown by streamlines with Re = 800 and $\alpha = 20^\circ$ at $t = 5$ (top) and $t = 10$ (bottom).

where the subscript α denotes the direction of the particle speed. In the D3Q19 discrete Boltzmann, the macroscopic velocities are given as [51]

$$\begin{aligned} \boldsymbol{e}_\alpha &= (e_{\alpha x}, e_{\alpha y}, e_{\alpha z}) \\ &= \begin{cases} (0,0,0) & \alpha = 0 \\ (\pm 1,0,0),(0,\pm 1,0),(0,0,\pm 1) & \alpha = 1-6 \\ (\pm 1,\pm 1,0),(\pm 1,0,\pm 1),(0,\pm 1,\pm 1) & \alpha = 7-18 \end{cases}. \end{aligned} \tag{45}$$

The equilibrium distribution function is defined as

$$f_\alpha^{\mathrm{eq}} = w_\alpha \left\{ p + p_0 \left[3\frac{\boldsymbol{e}_\alpha \cdot \boldsymbol{u}}{c^2} + \frac{9}{2}\frac{(\boldsymbol{e}_\alpha \cdot \boldsymbol{u})^2}{c^4} - \frac{3}{2}\frac{|\boldsymbol{u}|^2}{c^2} \right] \right\}, \tag{46}$$

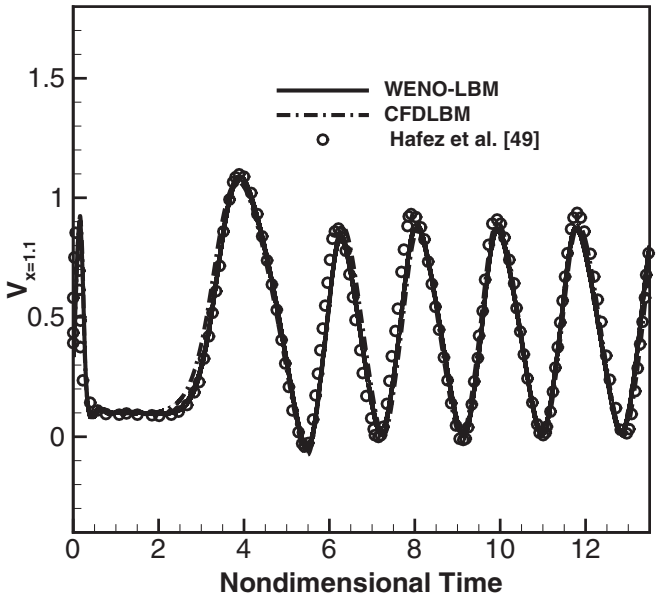

FIG. 30. Comparison of temporal development of v-velocity component at $(x/c, y/c) = (1.1, 0.0)$ for the NACA0012 hydrofoil with Re $= 800$ and $\alpha = 20^\circ$.

where w_α for the D3Q19 model is given by

$$w_0 = 1/3,$$
$$w_1 = \cdots = w_6 = 1/18,$$
$$w_7 = \cdots = w_{18} = 1/36. \tag{47}$$

and the pressure p and the velocity $\boldsymbol{u}$ are obtained from the following relations:

$$p = \sum_\alpha f_\alpha, \quad p_0 \boldsymbol{u} = \sum_\alpha \boldsymbol{e}_\alpha f_\alpha. \tag{48}$$

Now, the spatial derivatives in the 3D LB equation (44) can be discretized by the WENO scheme and the temporal term can be discretized by either the fourth-order explicit Runge-Kutta method or the implicit-explicit method, as described in Sec. IV.

VIII. CONCLUSION

In this study, a weighted essentially nonoscillatory finite-difference LBM solver for computing 2D incompressible flows in the generalized curvilinear coordinate is applied and assessed. The spatial derivatives in the LB equation in the computational domain are discretized using the fifth-order WENO scheme. Different test cases including the unsteady Taylor-Green vortex, unsteady doubly periodic shear layer flow, steady flow in a 2D cavity, steady cylindrical Couette flow, steady flow over a 2D circular cylinder, and steady and unsteady flows over a NACA0012 hydrofoil are simulated to investigate the accuracy and performance of the high-order WENOLBM applied. Some conclusions and remarks regarding the present study are as follows:

(1) It is shown that the results obtained by applying the WENO finite-difference LBM (WENOLBM) are in good agreement with the analytical solutions and the available numerical and experimental results for the problems simulated. By the implementation of the WENOLBM in the generalized curvilinear coordinates, curved geometries with nonuniform grids can be straightforwardly handled and thus an accurate solution of incompressible flows over practical geometries can be achieved.

(2) Two different time integration schemes, namely, the first-order implicit-explicit Runge-Kutta (IMEX) scheme and the fourth-order Runge-Kutta (RK4) explicit scheme are applied for the discretization of the temporal term. The numerical experiments for the cavity problem show that the IMEX WENOLBM is more stable compared to the RK4 WENOLBM scheme. This benefit in the IMEX scheme is due to the implicit time discretization of the collision term that causes the restriction of $\Delta t \leqslant 2\tau$ to be relaxed and the only restriction on Δt is due to the explicit discretization of the convective terms. As the Reynolds number increases, the benefit of using the IMEX scheme becomes more noticeable compared to the RK4 scheme.

(3) A sensitivity study is performed to examine the effect of numerical parameters on the accuracy of the solution obtained by applying the WENOLBM. The study indicates that by considering a small value of the reference (characteristic) velocity to reduce the compressibility effects, the fifth-order accuracy of the numerical method implemented is verified when estimating the error based on the analytical solution. Note that the fifth-order accuracy of the numerical method applied is achieved independent of the value of the reference velocity when the error is calculated based on the solution of the most refined grid.

(4) To show the accuracy and efficiency of the WENOLBM applied, the results are compared with the developed second-order central-difference finite-volume lattice Boltzmann method (FVLBM). The study indicates that the WENOLBM solver developed provides more accurate solutions than the FVLBM solver for the same mesh used. It is shown that for a specified accuracy, the WENOLBM applied needs a coarser mesh and the computation time is greatly reduced compared to the FVLBM.

(5) To more assess the accuracy and robustness of the WENOLBM, the results obtained are also compared and verified with those of the high-order compact finite-difference LBM (CFDLBM). It is demonstrated that both the solution procedures give nearly the same results for the same mesh utilized. The main advantage of the formulation of the WENOLBM over the CFDLBM is that there is no need to apply any numerical dissipation or filtering procedure and the solution algorithm is stable even at high Reynolds number flows.

(6) The study shows that the present solution procedure is robust, efficient, and accurate for solving steady and unsteady incompressible flows. Results obtained by the present solution are comparable with those of Navier-Stokes solvers with the note that the implementation of the WENO finite-difference LBM is much simpler; thus it may be considered as a suitable alternative flow solver to high-order WENO finite-difference Navier-Stokes solvers for studying more practical problems in which high-order accuracy solutions are needed to precisely represent flow physics.

ACKNOWLEDGMENT

The authors would like to thank Sharif University of Technology for the support of this research.

[1] X. He and L.-S. Luo, Theory of the lattice Boltzmann method: from the Boltzmann equation to the lattice Boltzmann equation, Phys. Rev. E **56**, 6811 (1997).

[2] X. He, G. D. Doolen, and T. Clark, Comparison of the lattice Boltzmann method and the artificial compressibility method for Navier-Stokes equations, J. Comput. Phys. **179**, 439 (2002).

[3] F. Dubois, P. Lallemand, C. Obrecht, and M. M. Tekitek, Lattice Boltzmann model approximated with finite difference expressions, Comput. Fluids (2016), doi:10.1016/j.compfluid.2016.04.013.

[4] P. Asinari, T. Ohwada, E. Chiavazzo, and A. F. D. Rienzo, Link-wise artificial compressibility method, J. Comput. Phys. **231**, 5109 (2012).

[5] P. J. Dellar, Incompressible limits of lattice Boltzmann equations using multiple relaxation times, J. Comput. Phys. **190**, 351 (2003).

[6] M. Geier, A. Greiner, and J. G. Korvink, Cascaded digital lattice Boltzmann automata for high Reynolds number flow, Phys. Rev. E **73**, 066705 (2006).

[7] R. Mei and W. Shyy, On the finite difference-based lattice Boltzmann method in curvilinear coordinates, J. Comput. Phys. **143**, 426 (1998).

[8] J. Tolke, M. Krafczyk, M. Schulz, and E. Rank, Implicit discretization and nonuniform refinement approaches for FD discretizations of LBGK models, Int. J. Mod. Phys. C **09**, 1143 (1998).

[9] Z. Guo and T. S. Zhao, Explicit finite-difference lattice Boltzmann method for curvilinear coordinates, Phys. Rev. E **67**, 066709 (2003).

[10] V. Sofonea and R. F. Sekerka, Viscosity of finite difference lattice Boltzmann models, J. Comput. Phys. **184**, 422 (2003).

[11] M. Watari and M. Tsutahara, Two-dimensional thermal model of the finite-difference lattice Boltzmann method with high spatial isotropy, Phys. Rev. E **67**, 036306 (2003).

[12] A. Xu, Finite-difference lattice-Boltzmann methods for binary fluids, Phys. Rev. E **71**, 066706 (2005).

[13] L. Wu, M. Tsutahara, and S. Tajiri, Finite difference lattice Boltzmann method for incompressible Navier-Stokes equation using acceleration modification, J. Fluids Sci. Technol. **2**, 35 (2007).

[14] S. C. Fu, R. M. C. So, and W. W. F. Leung, Stochastic finite difference lattice Boltzmann method for steady incompressible viscous flows, J. Comput. Phys. **229**, 6084 (2010).

[15] K. Hejranfar and E. Ezzatneshan, A high-order compact finite difference lattice Boltzmann method for simulation of steady and unsteady incompressible flows, Int. J. Numer. Methods Fluids **75**, 713 (2014).

[16] K. Hejranfar and E. Ezzatneshan, Implementation of a high order compact finite difference lattice Boltzmann method in generalized curvilinear coordinates, J. Comput. Phys. **267**, 28 (2014).

[17] H. Chen, Volumetric formulation of the lattice Boltzmann method for fluid dynamics: Basic concept, Phys. Rev. E **58**, 3955 (1998).

[18] H. Xi, G. Peng, and S.-H. Chou, Finite volume lattice Boltzmann method, Phys. Rev. E **59**, 6202 (1999).

[19] S. Ubertini, G. Bella, and S. Succi, Unstructured lattice Boltzmann method: Further development, Phys. Rev. E **68**, 016701 (2003).

[20] M. Stiebler, J. Tolke, and M. Krafczyk, An upwind discretization scheme for the finite volume lattice Boltzmann method, Comput. Fluids **35**, 814 (2006).

[21] V. Patil and K. N. Lakshmisha, Finite volume TVD formulation of lattice Boltzmann simulation on unstructured mesh, J. Comput. Phys. **228**, 5262 (2009).

[22] T. Lee and C.-L. Lin, A characteristic Galerkin method for discrete Boltzmann equation, J. Comput Phys. **171**, 336 (2001).

[23] Y. Li, E. J. LeBoeuf, and P. K. Basu, Least-squares finite-element scheme for the lattice Boltzmann method on an unstructured mesh, Phys. Rev. E **72**, 046711 (2005).

[24] X. Shi, J. Lin, and Z. Yu, Discontinuous Galerkin spectral element lattice Boltzmann method on triangular element, Int. J. Numer. Methods Fluids **42**, 1249 (2003).

[25] A. Duster, L. Demkowicz, and E. Rank, High-order finite elements applied to the discrete Boltzmann equation, Int. J. Numer. Methods Eng. **67**, 1094 (2006).

[26] M. Min and T. Lee, A spectral-element discontinuous Galerkin lattice Boltzmann method for nearly incompressible flows, J. Comput. Phys. **230**, 245 (2011).

[27] K. Hejranfar and M. Hajihassanpour, Chebyshev collocation spectral lattice Boltzmann method for simulation of low-speed flows, Phys. Rev. E **91**, 013301 (2015).

[28] P. R. Rao and L. A. Shaefer, Numerical stability of explicit off-lattice Boltzmann schemes: a comparative study, J. Comput. Phys. **285**, 251 (2015).

[29] Y. Wang, Y. L. He, T. S. Zhao, G. H. Tang, and W. Q. Tao, Implicit explicit finite difference lattice Boltzmann method for compressible flows, Int. J. Mod. Phys. C **18**, 1961 (2007).

[30] A. Nejat and V. Abdollahi, A critical study of the compressible lattice Boltzmann methods for Riemann problem, J. Sci. Comput. **54**, 1 (2013).

[31] P. Bhatnagar, E. P. Gross, and M. Krook, A model for collision processes in gases I: Small amplitude processes in charged and neutral one-component systems, Phys. Rev. **94**, 511 (1954).

[32] X. He and L. Luo, Lattice Boltzmann model for incompressible Navier-Stokes equation, J. Stat. Phys. **88**, 927 (1997).

[33] L. S. Luo, Theory of the lattice Boltzmann method: Lattice Boltzmann models for nonideal gases, Phys. Rev. E **62**, 4982 (2000).

[34] G. S. Jiang and C. W. Shu, Efficient implementation of weighted ENO scheme, J. Comput. Phys. **126**, 202 (1996).

[35] G. I. Taylor, On the decay of vortices in a viscous fluid, Philos. Mag., Ser. 6 **46**, 671 (1923).

[36] G. Noventa, F. Massa, F. Bassi, A. Colombo, N. Franchiana, and A. Ghidoni, A high-order discontinuous Galerkin solver for unsteady incompressible turbulent flows, Comput. Fluids **139**, 248 (2016).

[37] M. L. Minion and D. L. Brown, Performance of under-resolved two-dimensional incompressible flow simulations II, J. Comput. Phys. **138**, 734 (1997).

[38] P. J. Dellar, Bulk and shear viscosities in lattice Boltzmann equations, Phys. Rev. E **64**, 031203 (2001).

[39] K. A. Hoffmann and S. T. Chiang, *Computational Fluid Dynamics* (Engineering Education System, Wichita, KS, 2000), Vol. 1.

[40] U. Ghia, K. N. Ghia, and C. T. Shin, High-Re solutions for incompressible flow using the Navier-Stokes equations and a multigrid method, J. Comput. Phys. **48**, 387 (1982).

[41] A. Tiwari and S. P. Vanka, A ghost fluid lattice Boltzmann method for complex geometries, Int. J. Numer. Methods Fluids **69**, 481 (2011).

[42] M. Coutanceau and R. Bouard, Experimental determination of the main features of the viscous flow in the wake of a circular cylinder in uniform translation. Part I. Steady flow, J. Fluid Mech. **79**, 231 (1977).

[43] D. J. Tritton, Experiments on the flow past a circular cylinder at low Reynolds numbers, J. Fluid Mech. **6**, 547 (1959).

[44] S. C. R. Dennis and G. Z. Chang, Numerical solutions for steady flow past a circular cylinder at Reynolds number up to 100, J. Fluid Mech. **42**, 471 (1970).

[45] F. Nieuwstadt and H. B. Keller, Viscous flow past circular cylinders, Comput. Fluids **1**, 59 (1973).

[46] X. He, L. S. Luo, and M. Dembo, Some progress in lattice Boltzmann method. Part 1. Nonuniform mesh grids, J. Comput. Phys. **129**, 357 (1996).

[47] T. Imamura, K. Suzuki, T. Nakamura, and M. Yoshida, Acceleration of steady-state lattice Boltzmann simulations on non-uniform mesh using local time step method, J. Comput. Phys. **202**, 645 (2005).

[48] A. S. Grove, F. H. Shair, E. E. Petersen, and A. Acrivos, An experimental investigation of the steady separated flow past a circular cylinder, J. Fluid Mech. **19**, 60 (1964).

[49] M. Hafez, A. Shatalov, and M. Nakajima, Improved numerical simulations of incompressible flows based on viscous/inviscid interaction procedures, Comput. Fluids **36**, 1588 (2007).

[50] T. Imamura, K. Suzuki, T. Nakamura, and M. Yoshida, Flow simulation around an airfoil by lattice Boltzmann method on generalized coordinates, AIAA J. **43**, 1968 (2005).

[51] M. Hecht and J. Harting, Implementation of on-site velocity boundary conditions for D3Q19 lattice Boltzmann Simulations, J. Stat. Mech. (2010) P01018.